Acta Materialia 246 (2023) 118697

Contents lists available at ScienceDirect

Acta Materialia

journal homepage: www.elsevier.com/locate/actamat

Composition-dependent shuffle-shear coupling and shuffle-regulated strain glass transition in compositionally modulated Ti-Nb alloys

Yunting Su [a], Chuanxin Liang [a,*], Xun Sun [a], Hualei Zhang [a], Qianglong Liang [a], Yufeng Zheng [b], Yulin Hao [c], Rui Yang [c], Dong Wang [a,*], Dipankar Banerjee [d], Yunzhi Wang [e,*]

[a] Center of Microstructure Science, Frontier Institute of Science and Technology, State Key Laboratory for Mechanical Behavior of Materials, Xi'an Jiaotong University, Xi'an, Shaanxi, China
[b] Department of Chemical and Materials Engineering, University of Nevada Reno, Reno, NV 89557, USA
[c] Shenyang National Laboratory for Materials Science, Institute of Metal Research, Chinese Academy of Science, Shenyang, Liaoning, China
[d] Department of Materials Engineering, Indian Institute of Science, Bengaluru, Karnataka 560012, India
[e] Department of Materials Science and Engineering, The Ohio State University, Columbus, OH, USA

ARTICLE INFO

Keywords:
Martensitic transformations
Atomic shuffle
Spinodal decomposition
Ti-Nb shape memory alloys
Computer simulation

ABSTRACT

Athermal pure shuffle O′ nanodomains have been reported as a common structural state in metastable β-Ti alloys. In this study, by integrating thermodynamic databases, first-principles calculations, phase field simulations, and experiments, we reveal the coupling between the shuffle (O′) and shear (α″, orthorhombic martensite) nanodomains as a function of Nb concentration in Ti-Nb alloys. In particular, our first-principles calculations suggest a change in the phase transformation path from β → α″ to β → O′ as the Nb concentration increases, and our CALPHAD calculations based on the available thermodynamic database show a large metastable miscibility gap in Ti-Nb. Informed by these findings, our phase field simulations demonstrate how the O′ and α″ nanodomains form and evolve upon cooling in compositionally modulated Ti-Nb alloys produced by spinodal decomposition and the corresponding transformation behavior. Finally, our experimental characterization shows a continuous change of the shuffle component across the O′/α″ nanodomain boundaries. The novel microstructural states and their unique phase transformation path lead to an unprecedented continuous transformation behavior accompanied by superelasticity with almost zero hysteresis and small residual strain over a wide temperature range, all of which have been observed in the experiments. This unique transformation behavior upon cooling can be well characterized as a shuffle-regulated strain glass transition. This study could provide new insight in alloy design by utilizing composition-dependent shuffle-shear coupling during a structural phase transformation.

1. Introduction

As one class of multifunctional metastable β-Ti alloys, Ti-Nb-based shape memory alloys (SMAs) have become promising candidates for many advanced biomedical applications [1,2] due to their excellent biocompatibility and unique physical and mechanical properties including superelasticity over a wide temperature range [3–5], low modulus [6–8], high strength and good ductility [8], and tunable thermal expansion [9–11]. These properties are mainly attributed to the modification of the martensitic transformation (MT) behavior through composition optimization [11,12], thermo-mechanical processing [13,14], and training [15,16]. As a typical Ti-Nb-based SMA, Ti-24.2Nb-3.96Zr-8.1Sn (wt.%, Ti2448 for short) has shown unique superelasticity from 4.2 K to 400 K, tunable thermal expansion, and ultra-low Young's modulus [3,4,7,9]. So far, several mechanisms have been proposed to link phase transformations in Ti2448 and its unique mechanical and functional properties.

In view of the phase transformations in Ti2448, normal α″martensite (orthorhombic) has not been detected even at 100 K by 2D synchrotron X-ray diffraction (SXRD) measurement [4]. Concentration modulations of nanoscale (~5 nm) Nb-lean and Nb-rich regions have been detected through 3D atom probe tomography (APT) [3,4]. A reversible atomic rearrangement mechanism was proposed based on the concentration modulations, which describes a continuous change of crystal structure (i.e., lattice shear and shuffle) along the Burgers path between bcc and hcp crystals with orthorhombic symmetry upon cooling or loading [9,

* Corresponding authors.
E-mail addresses: liangcx@xjtu.edu.cn (C. Liang), wang_dong1223@xjtu.edu.cn (D. Wang), wang.363@osu.edu (Y. Wang).

https://doi.org/10.1016/j.actamat.2023.118697
Received 26 October 2022; Received in revised form 4 January 2023; Accepted 9 January 2023
Available online 14 January 2023

17,18]. Hao et al. reported the concentration dependence of Young's modulus and transformation strain [4] and proposed that the elastic confinement caused by the nanoscale concentration modulations could induce a continuous martensitic transformation (MT) that is responsible for the superelasticity observed over a wide temperature range [3]. Liu et al. showed stress-induced nanosized α″ and δ (orthorhombic) martensites in different regions under tensile loading, which may have contributed to the unique mechanical properties of the alloy [19].

It is well known that chemical inhomogeneities would influence the MT start temperature M_s [20–24] and transformation strain ε_{MT} [23,25]. In Ti-Nb binary alloys, it was reported that the increase of Nb content could change the phase transformation behavior from normal MT to strain glass transition [21] that produces nanodomains of martensite. Structural nanodomains have been reported in as-quenched metastable β-Ti alloys such as Ti-(26–29)Nb (at.%) [26], Ti-Nb-Zr alloys [27,28], Ti-Nb-O alloys [13,29], Ti-Nb-Zr-Ta-O alloys [10,11,24,30], Ti-18Mo (wt.%) [31], Ti-18Mo-5Al (wt.%) [27,32], and Ti-5Al-5Mo-5V-3Al (wt.%, Ti5553) [33]. These structural nanodomains have been thought to be α″ martensite because α″ and O′ phases have shown the same diffraction pattern [10,27,31,34] and the lattice shear associated with the nanoscale α″ domains is difficult to measure. Recently, a novel β (BCC) → O′ (orthorhombic) shuffle-only nanodomain → α″ (orthorhombic) martensitic nanodomain transition has been observed with continuous increase in lattice strain upon cooling from the room temperature to 87 K [34]. The β → α″ MT in metastable Ti-alloys is accomplished by a $\{2\bar{1}1\}\langle\bar{1}\bar{1}1\rangle_\beta$ lattice shear and an $\{011\}\langle 0\bar{1}1\rangle_\beta$ atomic shuffle [35,36], while the appearance of the shuffle dominated intermediate state of the O′ phase implies that the atomic shuffle precedes the shear [27,34,35,37]. Although the O′ phase has the same shuffle direction as that of the α″ phase, the shear value of the O′ phase is almost zero [34]. Thus, the O′ phase can be defined as a shuffle-dominated phase, which has been reported to be a common structural state in metastable β-Ti alloys [27,29,31–33,38]. Especially, the reported O′ nanodomains through sophisticated TEM characterizations of Ti-Mo [31], Ti5553 [33], and Ti2448 [34,39] alloys agree with this viewpoint. It was also found that the O′ nanodomains may improve the mechanical properties by influencing the formation of $\{332\}\langle 113\rangle_\beta$ deformation twins and transforming to α″ martensite under cold-rolling [40].

Previous work has shown that there exist miscibility gaps in Ti-Nb [41,42], Ti-Mo [41,43], and Ti-V [44,45] systems that have exhibited structural nanodomains, and the addition of a third element could enlarge the miscibility gap region or increase the driving force [28,45,46]. Phase field simulations have predicted the influence of the wavelength and amplitude of concentration modulations produced by spinodal decomposition on MT in Ti2448 [15,47], and reproduced the non-hysteretic superelasticity with the formation of nanoscale martensitic twin structures. The Burgers path has shown that both shuffle and shear are involved in the β → α″ transformation [48]. Theoretical studies and experimental observations have found that the Nb content could influence the shear and shuffle values [23,49,50], but the sequence of shuffle and shear (i.e., which one proceeds which) is still unclear. Two puzzles remain in metastable β-Ti alloys: (i) how do the shuffle nanodomains form? (ii) why do the shuffle domains maintain nanoscale (i.e., do not grow and coarsen) and transform to α″ upon cooling or loading?

In this study, we reveal the relationship among the concentration modulations, O′ nanodomains, and α″ nanodomains by integrating CALPHAD modeling, first-principles calculations, phase field simulations, and experiments. Based on the CALPHAD database, we first carry out phase field simulations to study spinodal decomposition and concentration modulation development in Ti-Nb binary systems, in particular, the amplitude and the wavelength of concentration modulation as a function of cooling rate. We then use first-principles calculations to show a concentration-dependent coupling between the shuffle and shear components, and the phase transformation path changes from β → α″ to β → O′ with increasing Nb concentration. Based on the phase transformation path revealed by the first principles calculations, we formulate a phase field model of shuffle plus shear structural transformation to study the relationship between the spatial distribution of Nb and the formation of O′ and α″ nanodomains. The calculations reveal a continued formation and growth of shuffle domains (O′) in the Nb-lean (but with Nb content ≥ 25 at.%) nanodomains in the β matrix at relatively high temperatures, and continued formation and growth of martensitic domains (α″) within the existing O′ domains upon further cooling. Finally, we show by experimental characterization a continuous change of the shuffle component across the O′/α″ nanodomain boundaries. We conclude that it is the stress-induced continuous O′ nanodomain to α″ nanodomain transition at different temperatures that leads to the linear-superelasticity over a wide temperature range.

2. Methods

2.1. CALPHAD modeling

According to the CALPHAD database [42], the Gibbs free energy of phase ϕ (ϕ = β (bcc) or α (hcp)) in Ti-Nb based on a substitutional solution model is given by:

$$G^{\phi} = x_{Nb}{}^{0}G^{\phi}_{Nb} + x_{Ti}{}^{0}G^{\phi}_{Ti} + RT\left[x_{Nb}\ln x_{Nb} + x_{Ti}\ln x_{Ti}\right] + x_{Nb}x_{Ti}I^{\phi} \quad (1)$$

where x_{Nb} and x_{Ti} denote the mole fractions of Nb and Ti, respectively, ${}^{0}G^{\phi}_{Nb}$ and ${}^{0}G^{\phi}_{Ti}$ are the Gibbs free energies of pure elements Nb and Ti in the ϕ state [51], respectively, R and T are the gas constant and absolute temperature, respectively, I^{ϕ} is the interaction parameter and has a value of I^{α} = 11,742.4 J/mol and I^{β} = 13,045.3 J/mol [42], respectively.

Based on the above description, the free energy of the metastable β phase as a function of Nb concentration and temperature can be fitted to the following polynomial:

$$G^{\beta}(x_{Nb}, T) = \sum_{i=0}^{8}(a_i + b_i \cdot T)\cdot x_{Nb}^{i}, \quad 300\,\mathrm{K} \le T \le 1200\,\mathrm{K} \quad (2)$$

where a_i and b_i are constants (as listed in Table 1). According to this free energy model, the system has a metastable miscibility gap as shown in Fig. 1.

2.2. First-principles calculations

The exact muffin-tin orbitals (EMTO) [50,52] method is adopted to perform the first-principles calculations for the total energies of Ti-xNb (x = 0, 10, 12, 13, 15, 20, 25, and 30, in at.%) alloys. Both the

Table 1
The coefficients, a_i and b_i, in the chemical free energy polynomial.

a_0	a_1	a_2	a_3	a_4	a_5	a_6	a_7	a_8
−9.3E-8	13,045.3	−13,045.3	−0.00365	1.75703	−1.29371	1.75991	1.13718	0.01889
b_0	b_1	b_2	b_3	b_4	b_5	b_6	b_7	b_8
−0.08807	−38.7341	185.587	−809.998	2438.68	−4520.70	4974.02	−2971.82	742.956

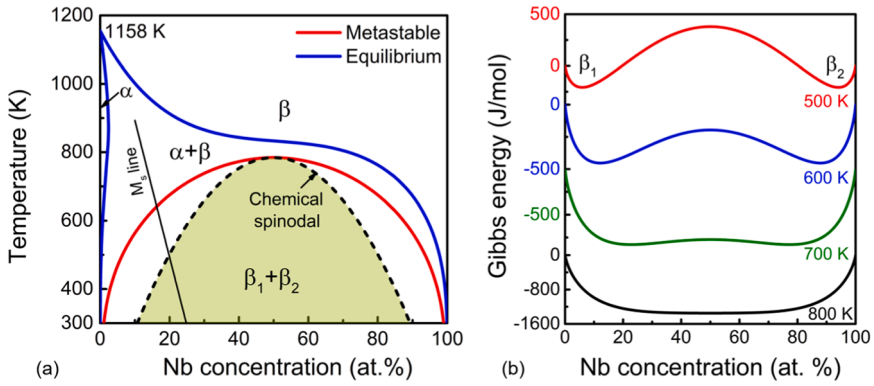

Fig. 1. (a) Calculated equilibrium phase diagram (blue solid lines) and metastable phase diagram considering only the β phase (red solid line), where the spinodal decomposition occurs within the regions (light green color) below the chemical spinodal. (b) Free energy curves of the metastable β phase at different temperatures. (For interpretation of the references to color in this figure legend, readers are referred to the web version of this article.)

self-consistent and total energy calculations are performed by the Perdew-Burke-Ernzerhof (PBE) generalized gradient approximation [53]. The scalar-relativistic approximation and soft-core approximation are used to solve the Kohn-Sham equation. The present alloys are considered non-magnetic. We use the coherent-potential approximation (CPA) [52] to deal with the random solid solution with a screening parameter of 0.6 [54]. To capture accurately the energy changes associated with structural transformations, we employ *k*-point meshes of 7 × 11 × 13 for the α″ phase and 29 × 29 × 29 for the β phase in the irreducible Brillouin zone after a convergency test. The equilibrium lattice constants are obtained by fitting the calculated total energies of the bcc structure by using a Morse-type function.

According to the Burgers orientation relationship for the bcc to hcp structural transformation [48], four variables should be considered in calculating the total energy along the β to α phase transition path, i.e., the Winger-Seitz radius (w, in Bohr), the axis ratios of c/a and b/a, and the shuffle vector η, where a, b and c are lattice parameters of the β, α, and α″ phases [55](see Fig. 3).

Theoretically, the energy difference $\Delta E_{\beta\to\alpha} = (E_\alpha - E_\beta)$ between the β and α phases increases from −0.8 to 3.0 mRy with increasing Nb content. Li et al. [49] found that the volume difference between the β and α phases is small (~1.5%), leading to a small absolute energy difference (less than 0.2 mRy) between the two phases associated with the volume change. Thus, the total energy difference caused by the volume difference between the β and α phases can be ignored. The energy difference caused by the volume difference between the β and α″ phases is expected to be even less than that between the β and α phases, since the α″ phase is considered as the intermediate phase between the β and α phases. Thus, to reduce the computation cost, we fix w as the equilibrium lattice constant of the bcc phase.

2.3. Phase field simulations

2.3.1. Spinodal decomposition in Ti-Nb binary alloys

The concentration modulations developed during spinodal decomposition is described by phase field simulations. The total free energy functional of the parent β phase of the Ti-Nb binary alloy system in the temperature range from 1173 K to 300 K is formulated based on the gradient thermodynamics [56,57] as:

$$F^{SD} = \int_V \left\{ G^{\beta}(x_{Nb}, T) + \frac{\kappa_x}{2}(\nabla x_{Nb})^2 \right\} dV \tag{3}$$

where $G^{\beta}(x_{Nb}, T)$ is the local bulk chemical free energy given by Eq. (2) and κ_x is the gradient energy coefficient. The time-evolution of x_{Nb} can be solved by the Cahn-Hilliard equation [58]:

$$\frac{\partial x_{Nb}}{\partial t} = \nabla\left[M\nabla\frac{\delta F^{SD}}{\delta x_{Nb}} \right] + \zeta_x \tag{4}$$

where ζ_x is the Langevin noise term characterizing thermal fluctuations [59,60], M is the chemical mobility, and is modeled using the CALPHAD method as [61]:

$$M = \frac{1}{RT}\exp\left(\frac{\phi}{RT}\right) \tag{5}$$

where $\phi = -Q + RT\ln(M^0)$ with Q as an activation enthalpy and M^0 as a frequency factor. In CALPHAD approach, ϕ is generally expressed by the Redlich-Kister polynomials [61,62]:

$$\phi = x_{Ti}\phi^{Ti} + x_{Nb}\phi^{Nb} + x_{Ti}x_{Nb}\sum_r {}^r\phi^{Ti,Nb}(x_{Ti} - x_{Nb})^r \tag{6}$$

where ϕ^{Ti}, ϕ^{Nb} are the mobility parameters for pure element Ti and Nb, respectively, and ${}^r\phi^{Ti,Nb}$ is binary interaction parameter for the β phase in the Ti-Nb binary system [63], and $r = 0, 1$. These mobility parameters are generally derived from extensive experimental diffusivities such as interdiffusivities, tracer diffusion coefficients, and impurity diffusion coefficients in the bcc Ti-Nb, thus the calculated interdiffusivities based on the M show a good fit to the experimental interdiffusivities in the bcc Ti-Nb [63,64]. Therefore, the chemical mobility M in Eq. (5) is effective to calculate the spinodal decomposition that is related to the interdiffusivity [58].

2.3.2. Martensitic transformation in Ti-Nb binary alloys

To describe the MT in Ti-Nb, structural order parameters characterizing the shuffle (η) and shear (φ) components of the transformation are considered in this study. There are 12 $\{011\}\langle 0\bar{1}1\rangle_\beta$ shuffle and 6 $\{2\bar{1}1\}\langle\bar{1}\bar{1}1\rangle_\beta$ shear modes for the β → α″ MT [35,36], and 12 $\{011\}\langle 0\bar{1}1\rangle_\beta$ shuffle modes for the β → O′ transformation [34], leading to 12 crystallographic equivalent α″ and O′ variants. Since the shuffle does not contribute to the transformation strain, only six transformation matrices are needed to describe the shear deformation [65]:

$$U_1=\begin{bmatrix}\frac{a_{\alpha''}}{a_\beta} & 0 & 0\\ 0 & \frac{b_{\alpha''}+c_{\alpha''}}{2\sqrt{2}a_\beta} & \frac{c_{\alpha''}-b_{\alpha''}}{2\sqrt{2}a_\beta}\\ 0 & \frac{c_{\alpha''}-b_{\alpha''}}{2\sqrt{2}a_\beta} & \frac{b_{\alpha''}+c_{\alpha''}}{2\sqrt{2}a_\beta}\end{bmatrix},\ U_2=\begin{bmatrix}\frac{a_{\alpha''}}{a_\beta} & 0 & 0\\ 0 & \frac{b_{\alpha''}+c_{\alpha''}}{2\sqrt{2}a_\beta} & \frac{b_{\alpha''}-c_{\alpha''}}{2\sqrt{2}a_\beta}\\ 0 & \frac{b_{\alpha''}-c_{\alpha''}}{2\sqrt{2}a_\beta} & \frac{b_{\alpha''}+c_{\alpha''}}{2\sqrt{2}a_\beta}\end{bmatrix},$$

$$U_3=\begin{bmatrix}\frac{b_{\alpha''}+c_{\alpha''}}{2\sqrt{2}a_\beta} & 0 & \frac{c_{\alpha''}-b_{\alpha''}}{2\sqrt{2}a_\beta}\\ 0 & \frac{a_{\alpha''}}{a_\beta} & 0\\ \frac{c_{\alpha''}-b_{\alpha''}}{2\sqrt{2}a_\beta} & 0 & \frac{b_{\alpha''}+c_{\alpha''}}{2\sqrt{2}a_\beta}\end{bmatrix},\ U_4=\begin{bmatrix}\frac{b_{\alpha''}+c_{\alpha''}}{2\sqrt{2}a_\beta} & 0 & \frac{b_{\alpha''}-c_{\alpha''}}{2\sqrt{2}a_\beta}\\ 0 & \frac{a_{\alpha''}}{a_\beta} & 0\\ \frac{b_{\alpha''}-c_{\alpha''}}{2\sqrt{2}a_\beta} & 0 & \frac{b_{\alpha''}+c_{\alpha''}}{2\sqrt{2}a_\beta}\end{bmatrix},$$

$$U_5=\begin{bmatrix}\frac{b_{\alpha''}+c_{\alpha''}}{2\sqrt{2}a_\beta} & \frac{c_{\alpha''}-b_{\alpha''}}{2\sqrt{2}a_\beta} & 0\\ \frac{c_{\alpha''}-b_{\alpha''}}{2\sqrt{2}a_\beta} & \frac{b_{\alpha''}+c_{\alpha''}}{2\sqrt{2}a_\beta} & 0\\ 0 & 0 & \frac{a_{\alpha''}}{a_\beta}\end{bmatrix},\ U_6=\begin{bmatrix}\frac{b_{\alpha''}+c_{\alpha''}}{2\sqrt{2}a_\beta} & \frac{b_{\alpha''}-c_{\alpha''}}{2\sqrt{2}a_\beta} & 0\\ \frac{b_{\alpha''}-c_{\alpha''}}{2\sqrt{2}a_\beta} & \frac{b_{\alpha''}+c_{\alpha''}}{2\sqrt{2}a_\beta} & 0\\ 0 & 0 & \frac{a_{\alpha''}}{a_\beta}\end{bmatrix}. \tag{7}$$

The lattice constants of the β and α″ phases, a_β= 3.285 Å, $a_{\alpha''}$= 3.178 Å, $b_{\alpha''}$= 4.182 Å, $c_{\alpha''}$= 4.635 Å in Ti-23 at.% Nb reported in the literature [55] are used in our simulations, and the corresponding stress-free transformation strain (SFTS) $\varepsilon^0_{ij}(p)$ is calculated using $\varepsilon^0_{ij}(p) = \frac{1}{2}\left(U_p^T U_p - I\right)$, $p = 1-6$ [66], where the superscript T indicates matrix transpose, and $\boldsymbol{I}$ is the identity matrix.

A coupling relationship between the shuffle (η) and shear (φ) is obtained from the first-principles calculations and used in our phase field simulations, i.e., $\varphi = \sum_{i=2,4,6,8} B_i \eta^i$, where B_i are coefficients and details are in Section 3.3. Therefore, the total free energy functional, F^{MT}, for the MT can then be expressed involving only the shuffle (η) as:

$$F^{MT} = \int d^3r\left[f_{ch}(\eta_p) + f_{gr}(\eta_p) + f_{ex}(\eta_p)\right] + E_{el},\ p = 1-6 \tag{8}$$

where the local chemical free energy f_{ch} is approximated by a Landau polynomial:

$$f_{ch}(\eta_p) = \frac{1}{2}A_1\sum_{p=1}^{6}\eta_p^2(\mathbf{r}) - \frac{1}{4}A_2\sum_{p=1}^{6}\eta_p^4(\mathbf{r}) + \frac{1}{6}A_3\left(\sum_{p=1}^{6}\eta_p^2(\mathbf{r})\right)^3 \tag{9}$$

where A_1 and A_2 are concentration-dependent expansion coefficients (details are given in Section 3.2), and A_3 is a constant. f_{gr} is the non-local gradient energy associated with spatial non-uniformities of the structural order parameters η_p:

$$f_{gr}\left(\eta_p\right) = \frac{1}{2}\kappa_\eta\sum_{p=1}^{6}\left(\nabla\eta_p\right)^2 \tag{10}$$

where κ_η is the gradient energy coefficient, and f_{ex} is the elastic energy caused by an external load:

$$f_{ex}\left(\eta_p\right) = -\sigma_{kl}\cdot\varepsilon^{MT}_{kl}(\mathbf{r}) \tag{11}$$

where σ_{kl} is the applied stress, $\varepsilon^{MT}_{kl} = \sum_{p=1}^{6}\varepsilon^0_{kl}(p)\varphi_p$ is the strain field, and E_{el} is the elastic strain energy associated with lattice mismatch between the parent and martensite phases and among different variants of the martensitic phase. It can be formulated [67] in a closed form under the homogeneous modulus assumption (i.e., the β and α″ phases are assumed to have the same elastic modulus) as:

$$E_{el} = \frac{1}{2}\sum_{p=1}^{6}\sum_{q=1}^{6}\int\frac{d^3k}{(2\pi)^3}B_{pq}(\boldsymbol{n})\{\varphi_p\}_k\{\varphi_q\}^*_k \tag{12}$$

where the integral is taken in the reciprocal space, $\boldsymbol{n} = \frac{\boldsymbol{k}}{k}$ is a unit vector and $\boldsymbol{k}$ is a vector with modulus k in the reciprocal space, $\{\varphi_p\}_k$ represents the Fourier transform of φ_p, $\{\varphi_p\}^*_k$ is the complex conjugate of $\{\varphi_p\}_k$. For a system with a fixed external boundary:

$$B_{pq}(\boldsymbol{n}) = \begin{cases} C_{ijkl}\varepsilon^0_{ij}(p,\mathbf{r})\varepsilon^0_{kl}(q,\mathbf{r}), n = 0 \\ C_{ijkl}\varepsilon^0_{ij}(p,\mathbf{r})\varepsilon^0_{kl}(q,\mathbf{r}) - n_i\sigma^0_{ij}(p,\mathbf{r})\Omega_{jk}(\boldsymbol{n})\sigma^0_{kl}(q,\mathbf{r})n_l,\ n \neq 0 \end{cases} \tag{13}$$

where C_{ijkl} is the elastic modulus tensor, $\sigma^0_{ij}(p,\mathbf{r}) = C_{ijkl}\varepsilon^0_{kl}(p,\mathbf{r})$ and $\Omega^{-1}_{ij}(\boldsymbol{n}) = C_{ijkl}n_k n_l$. When the contribution of external load is considered, a free external boundary is used, i.e., $B_{pq}(\boldsymbol{n})$=0 at $\boldsymbol{n} = 0$.

The stochastic time-dependent Ginsburg-Landau equation is used to describe the temporal evolution of the shuffle η:

$$\frac{\partial\eta_p(\mathbf{r},t)}{\partial t} = -L\frac{\delta F^{MT}}{\delta\eta_p(\mathbf{r},t)} + \zeta^\eta_p(\mathbf{r},t), p = 1-6 \tag{14}$$

where L is the structural mobility of the order parameters and $\zeta^\eta_p(\mathbf{r},t)$ is the Langevin noise term describing thermal fluctuations of the structural order parameters. The elastic constants of the parent phase C_{11} = 155.4 GPa, C_{12} =124.7 GPa, and C_{44} = 12.8 GPa reported in [68] are used in the simulations and assumed to be independent of concentration. The dimensionless gradient energy coefficient is chosen to be κ^*_c= 0.035 and κ^*_η= 0.05, describing a numerical grid size of l_o ~1 nm. The dimensionless structural mobility parameters are chosen as L^* = 1.0. The system size used in the simulations is $128l_o \times 128l_o \times 128l_o$. Periodic boundary conditions are applied along all three dimensions.

2.4. Experimental

The ingot of Ti-24.2Nb-3.96Zr-8.1Sn-0.2O alloy (Ti2448, wt.%) was fabricated in a vacuum arc melting furnace using a Ti-Sn master alloy with pure Ti, Nb, and Zr. The samples were wrapped in Ti foils and encapsulated in quartz tubes and solution treated at 1173 K for 30 min followed by water quenching (WQ) to room temperature by breaking the quarts tubes. After the solution treatment, some specimens were cold-rolled to 50% reduction in thickness. Thin foils for TEM analysis were prepared using a Dual-Bean Focused Ion Beam (DB-FIB) FEI Helios Nanolab 600 system. High angle annular dark field-scanning transition electron microscopy (HAADF-STEM) analysis was carried out using a probe-corrected FEI Titan3™ 80–300 operated at 300 kV, and the ImageJ software was used to plot the intensity profiles and calculate the shuffle and shear components recorded from the HAADF-STEM images.

3. Results

3.1. Nanoscale concentration modulation developed during cooling

Fig. 1(a) shows the equilibrium and metastable phase diagrams of the Ti-Nb binary system according to the thermodynamic description in Eq. (1), and the M_s line indicates where the β → α″ MT starts according to references [20–24]. In the current study, the metastable phase is considering only the β phase. There is a large metastable miscibility gap proposed as $\beta_1 + \beta_2$ below the β solvus, with a spinodal range between ~10 and ~90 at.% of Nb. Thermodynamically, the leanest equilibrium concentration for β_1 is ~1 at.% Nb and the richest equilibrium concentration for β_2 is ~99 at.% Nb. The free energy curves of the metastable β phase at different temperatures are shown in Fig. 1(b). Need to note that the ω phase may appear after water quenching in metastable

β-Ti alloys [38,42], which have shown an important influence on the mechanical properties. To isolate the effect of coupling between the β to O′/α″ transitions and to simplify our model, we have ignored the ω phase in the current work.

To characterize the concentration modulations developed by spinodal decomposition upon cooling, phase field simulations were carried out with different cooling rates for a homogeneous system of Ti-50 at.% Nb. Fig. 2(a, c) shows the three-dimensional (3D) simulation result of concentration modulations of Nb via water quenching (WQ, 200 K/s) and air cooling (AQ, 20 K/min) to 300 K, respectively. The one-dimensional (1D) concentration waves along the body-diagonal of the computational cell are shown in Fig. 2(b, d) for the WQ and AQ samples, respectively. Overall, the Nb-lean β_1 (blue color) and Nb-rich β_2 (red color) regions form a typical interpenetrated domain structure, and the amplitude and wavelength of the water-quenched sample are smaller than that of the air-cooled sample. In addition, there are no significant changes in the spatial distribution, concentration modulation amplitude, and wavelength below 500 K, which can be attributed to the low chemical mobility at low temperatures [63]. At 300 K, the Nb concentration varies in between ~25 and ~70 at.% in the WQ sample, while it varies in between ~20 and ~75 at.% in the AQ sample. Previous studies [69,70] have shown that the fast quenching in water or brine from high temperature range (single phase region) to room temperature cannot inhibit spinodal decomposition. For example, well defined periodic structure with a wavelength ~13 nm has been found via TEM in the solution-treated Cu-45Ni-15Cr (wt.%) alloy after iced water quenching to room temperature [71]. Concentration modulations of Nb and O have also been found via point-by-point binomial APT analysis in as-quenched Ti-23Nb-2O (at.%) alloy at room temperature [29]. Actually, when the system is quenched to a temperature within the chemical spinodal, the free energy will immediately decrease, small composition fluctuations with solute-rich and solute-lean regions can spontaneously form and grow, and the alloy will be unstable [72]. In the following study, the concentration modulations (~10 nm wavelength) obtained via WQ are used to systematically study the effect of concentration modulations on β → O′ → α″ transformations based on the water quenching process in the experiment [34].

3.2. Transformation path for bcc → orthorhombic structural transformation

The crystallographic relationships among the bcc (β), orthorhombic (O′, α″), and hcp (α or α′) crystal structures are shown in Fig. 3. The orientation relationship between the bcc (β) and hcp (α or α′) crystals can be described as $[011]_{bcc}//[0001]_{hcp}$ and $\langle 100\rangle_{bcc}//\langle 11\bar{2}0\rangle_{hcp}$ [73], while the lattice correspondence between the bcc (β) and orthorhombic (O′, α″) crystals is [23]:

$$[100]_{bcc}//[100]_{ortho},\ [011]_{bcc}//[010]_{ortho},\ [0\bar{1}1]_{bcc}//[001]_{ortho}.$$

As shown in Fig. 3, the b/a ratio and shuffle distance z vary with different phases. The β phase has the $b/a = c/a=\sqrt{2}$ and the shuffle distance $z = 0$, while the α (or α′) phase has the $b/a=\sqrt{3}$ and the shuffle distance $z=\frac{b}{6}$. The O′ and α″ could be considered as transitional phases between the β phase and α (or α′) phases. Both the β → O′ and β → α″ transformations require the same mode of atomic shuffle$\{011\}\langle 0\bar{1}1\rangle_{\beta}$, but the latter also requires a lattice shear of$\{2\bar{1}1\}\langle\bar{1}\bar{1}1\rangle_{\beta}$ [27,34]. The O′ phase has the $b/a = c/a=\sqrt{2}$ and $0<z<\frac{b}{6}$, while the α″ has the $\sqrt{2}<b/a<\sqrt{3}$ and $0<z<\frac{b}{6}$.

To capture the shuffle and shear components of the β → α″ structural transformation, first-principles calculations at 0 K are carried out to characterize the energy landscapes corresponding to the β → α″ transformation in Ti-xNb (x = 15, 20, 25, and 30, in at.%), which are plotted in Fig. 4 in the space of shear and shuffle components. Such energy landscapes show the equilibrium values of the shuffle and shear components (identified by the red dots) and thus the equilibrium structural states (either α′ (with complete shuffle and shear components), α″ (with partial shuffle and shear components) or O′ (with dominantly the shuffle component)), and the steepest energy decent paths (the yellow dashed lines) from β (with zero shear and shuffle components) to either α′ via O′, α″ via O′, or O′ alone as a function of Nb concentration. In these energy contour plots, the parent bcc crystal is chosen as the starting structural state and the final hcp crystal is chosen as the final structural state, so if both the shuffle and shear components are equal to 0, it represents the β phase, if both are equal to 1, it represents the α (or α′) phase, if both are between 0 and 1, it represents the α″ phase, and if only the shuffle component is in between 0 and 1 while the shear component is 0, it represents the O′ phase.

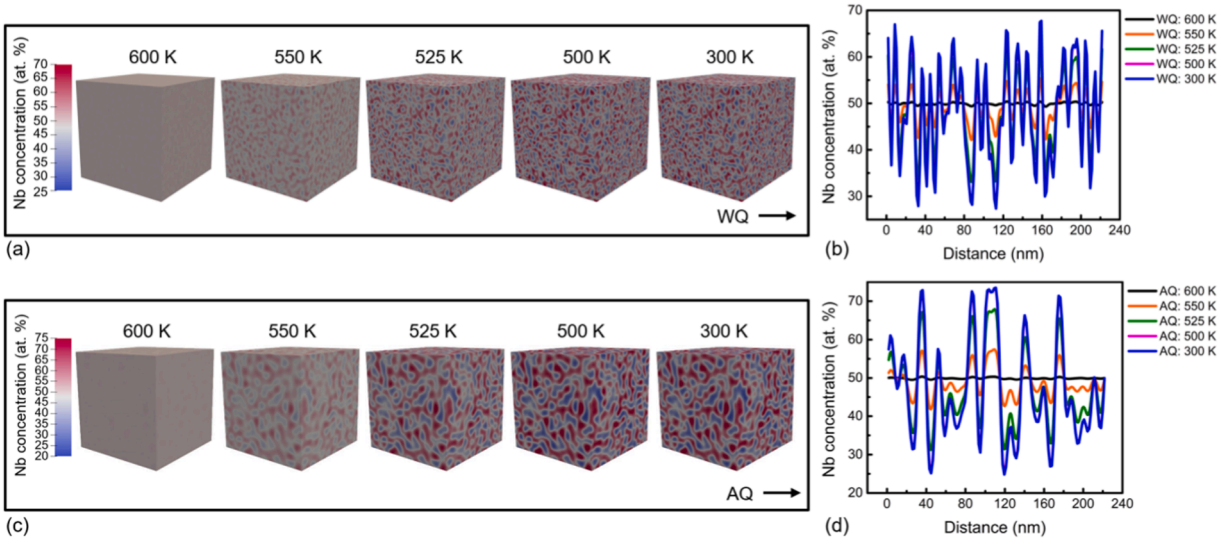

Fig. 2. Phase field simulation predictions of Nb concentration modulations generated by spinodal decomposition of β phase in Ti-50 at.% Nb during cooling. (a, c) Nb concentration distributions after water quenching (WQ) and air cooling (AQ), respectively, from 1173 K to 300 K, where the blue regions are the solute-lean β_1 phase regions and the red regions are the solute-rich β_2 phase regions. (b, d) 1D Nb concentration profiles along the body-diagonal of the 3D computational cells shown in (a, c). (For interpretation of the references to color in this figure legend, readers are referred to the web version of this article.)

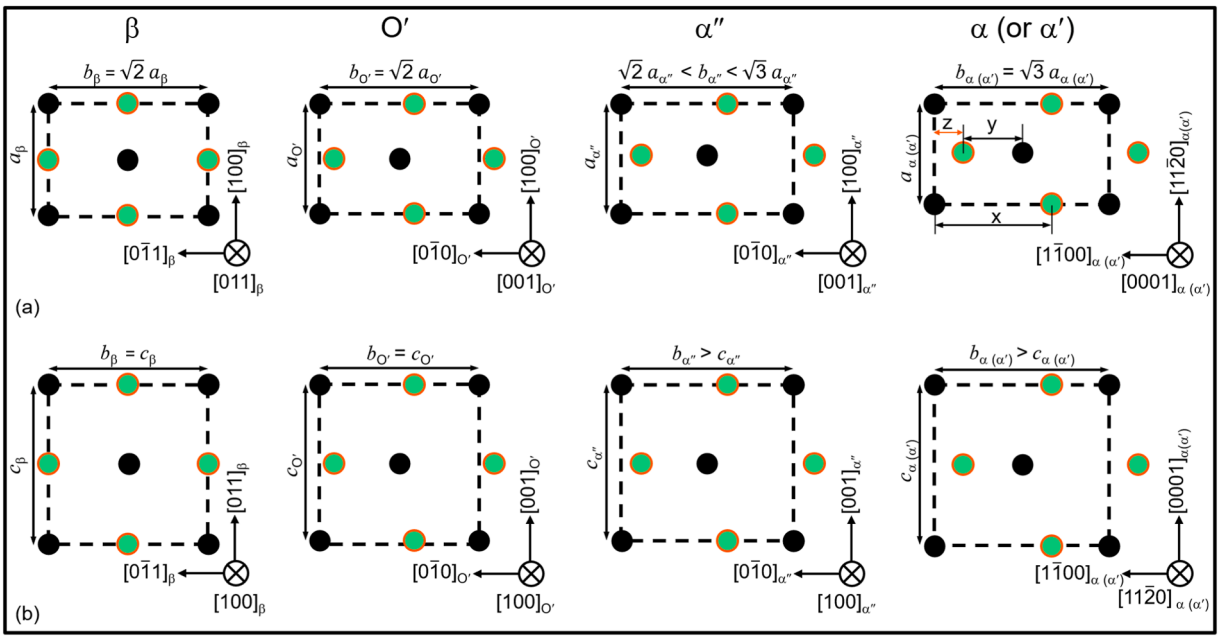

Fig. 3. Schematic drawing of lattice correspondence among the β, O′, α″, and α (or α′) phases: (a) at adjacent $(011)_{\beta}$, $(001)_{O'}$, $(001)_{\alpha''}$, $(0001)_{\alpha\ (or\ \alpha')}$ basal planes, (b) at adjacent $(100)_{\beta}$, $(100)_{O'}$, $(100)_{\alpha''}$, $(11\bar{2}0)_{\alpha\ (or\ \alpha')}$ basal planes.

The energy landscape shown in Fig. 4(a) indicates that the structural transformation in Ti-10 at.% Nb is β → α′ transformation via O′, the energy landscapes shown in Fig. 4(b–d) indicate that the structural transformations in Ti-*x*Nb (x = 15, 20 and 25 at.%) are β → α″ transformation via O′, and the energy landscape shown in Fig. 4(e) indicates that the structural transformation in Ti-30 at.% Nb is β → O′. All transformation paths shown in Fig. 4(a–d) indicate that the shuffle leads the shear, implying shuffle-regulated β → α′ or β → α″ transformations. The α″ phase is the stable phase in Ti-15 at.% Nb, Ti-20 at.% Nb and Ti-25 at.% Nb, but both the shear and shuffle components decrease with increasing Nb content. At high Nb concentration (Fig. 4(d)), the shear value almost vanishes while the shuffle value remains finite, leading to the appearance of shuffle only O′ phase. This could explain why the O′ phase can be detected experimentally before the α″ formation in Ti2448 alloy upon cooling [34]. When the Nb concentration is Ti-30 at.% Nb, the shear component decreases to zero, but the shuffle component remains finite at the minimum energy state, suggesting the appearance of the O′ phase and a change of the phase transformation path from β → α″ to β → O′.

Fig. 4(f) shows the theoretically calculated energy difference $\Delta E_{\beta\to\alpha'} = (E_{\alpha'} - E_{\beta})$, $\Delta E_{\beta\to\alpha''} = (E_{\alpha''} - E_{\beta})$ and $\Delta E_{\beta\to O'} = (E_{O'} - E_{\beta})$ between the metastable phases and the β phase as a function of Nb content in Ti-*x*Nb binary alloys at 0 K. The $\Delta E_{\beta\to\alpha''}$ increases from −1.28 to −0.16 mRy with increasing Nb content from Ti-15 at.% Nb to Ti-25 at.% Nb, which implies the decrease in the relative stability of the α″ phase with increasing Nb content. The same trend of the $\Delta E_{\beta\to\alpha''}$ has also been found in Ti-(18.75, 25) at.% Nb alloys [74] and Ti-(15, 20, 25, 30) at.% V alloys [75]. The low driving force (i.e., $\Delta E_{\beta\to\alpha''} = -0.16$ mRy) for Ti-25 at.% Nb could explain why the normal β → α″ MT cannot be experimentally found in Ti-25 at.% Nb and Ti2448 at room temperature [21, 34]. The existence of α″ strain glass in Ti-25 at.% Nb [21] and Ti2448 [34] may suggest the existence of concentration inhomogeneity or stress/strain field inhomogeneity. The lower energy difference ($\Delta E_{\beta\to O'} = -0.04$ mRy) at Ti-30 at.% Nb could further decrease the stability of α″ or O′, but the existence of O′ in solution-treated Ti-30 at.% Nb [76] and Ti2448 [38] at room temperature may indicates the existence of concentration inhomogeneity.

3.3. *Shuffle-shear relationship and transformation temperatures for β → O′ → α″ transformations*

Fig. 5(a) describes the shuffle and shear components corresponding to the energy-minimum states at different Nb concentrations. The energy-minimum state for pure Ti corresponds to α phase, and the energy-minimum states for Ti-*x*Nb ($x \le 12$ at.%) correspond to α′ phase, and that for Ti-*x*Nb (12 at.% $< x \le$ 25 at.%) correspond to α″ phase. This result also shows that the shear component decreases to zero but the shuffle component remains finite for Ti-30 at.% Nb, thus the minimum energy state of Ti-30 at.% Nb corresponds to the O′ phase. The minimum energy states (marked by the filled red circles in Fig. 4) in the four different Ti-*x*Nb (x = 15, 20, 25, 30 at.%) alloys are shown together in Fig. 5(b), and the dashed curve traces the energy minima (the equilibrium structural states) in the shear-shuffle space as a function of the Nb content. Based on the above results, the shear and shuffle components at the equilibrium structural states can be coupled, and the following nonlinear relationship between the degree of shear (φ) and degree of shuffle (η) for the β → α″ and β → O′ transformations obtained from the ab initio calculation results is used in our phase field model and shown in Fig. 5(c):

$$\varphi = -0.32802 \times \eta^2 + 19.14168 \times \eta^4 - 63.13645 \times \eta^6 + 66.1991 \times \eta^8 \quad (15)$$

where the degree of shuffle (η) is selected as the independent order parameter and is quantified by $z/b=((x\text{-}y)/2)/b$, where z is the shuffle distance (Fig. 3). The degree of shear (φ) is selected as a dependent order parameter, which is defined by b/a ratio (Fig. 3) and determined by the value of η. From the definition of the shuffle and shear components, η=0 and φ=0 represent the β (bcc) phase, and η≠0 and φ≠0 represent the α″ phase. Need to note that η=1 and φ=1 represent an hcp structure. $\eta_c \approx 0.2$ is the critical value that separates the O′ (η≠0, φ=0) and α″ (η≠0, φ≠0), as shown in Fig. 5(b, c). Indeed, shear component showed a continuous increase upon cooling from 293 K to 87 K in Ti2448 alloy [34], which suggests a similar effect of temperature on the shuffle and shear components like the effect of Nb concentration on the shuffle and shear components obtained by the first-principles calculations at 0 K. Thus, in our phase field simulations, the β → O′ → α″ transformations in

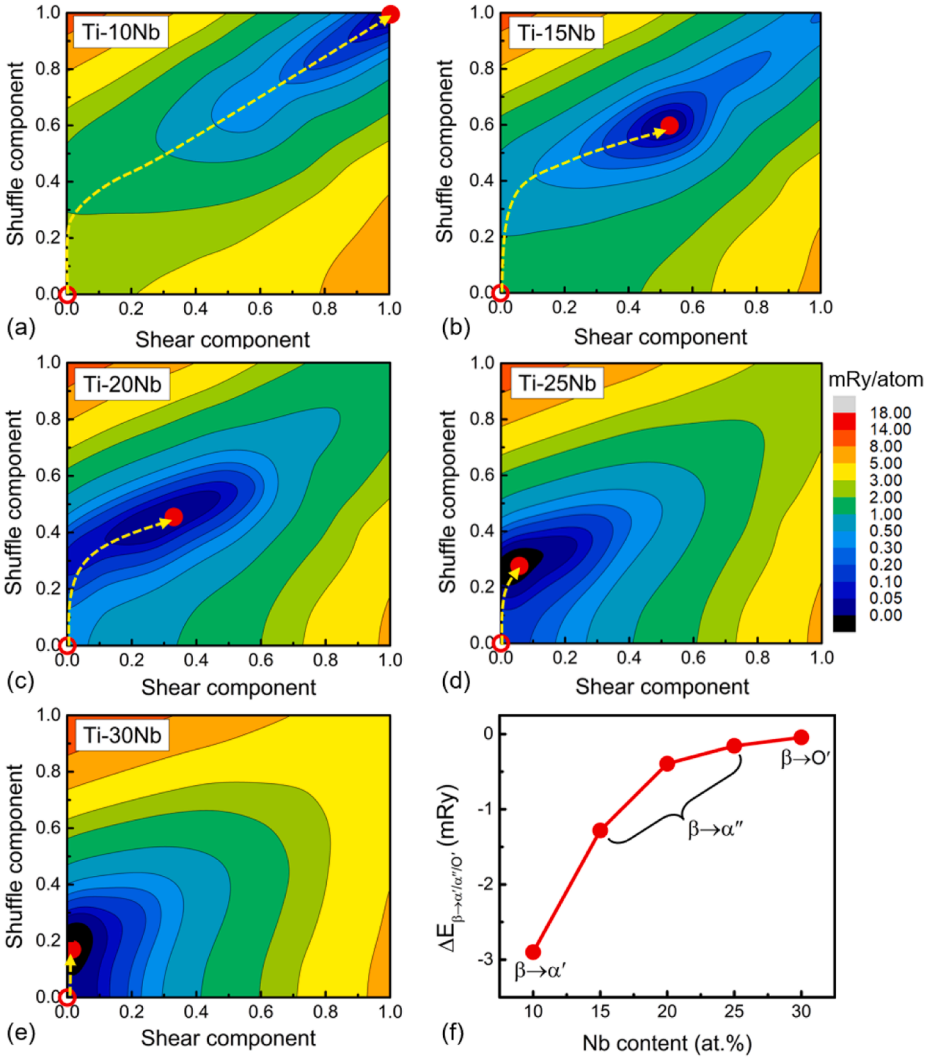

Fig. 4. Energy landscapes of β → α′, β → α″ and β → O′ transformations for Ti-*x*Nb (at.%) as a function of the shear and shuffle components: (a) $x = 10$, (b) $x = 15$, (c) $x = 20$, (d) $x = 25$, (e) $x = 30$. All energies are plotted relative to the corresponding energy of the α″ phase. The shuffle mode is $(011)[0\bar{1}1]_{\beta}$, and the shear mode is $(2\bar{1}1)[11\bar{1}]_{\beta}$. The red open circles represent the β phase, and the red filled circles represent the positions with minimum energy at different Nb concentrations. (f) Theoretical energy difference ($\Delta E_{\beta\to\alpha'}$, $\Delta E_{\beta\to\alpha''}$, and $\Delta E_{\beta\to O'}$, in mRy) as a function of Nb content. (For interpretation of the references to color in this figure legend, readers are referred to the web version of this article.)

Ti-Nb alloys are characterized by 6 non-conserved structural order parameters, i.e., η_p ($p = 1-6$), with positive and negative values describing the 12 shuffle modes (i.e., 12 variants of the O′ phase). The 12 shuffle modes and 6 shear order parameters φ_p ($p = 1-6$) describe 12 variants of the α″ phase. The state with $|\eta_{p\ =\ 1\sim6}| = 0$ represents the parent β phase, $0 < |\eta_p| \le 0.2$ and $\varphi_p = 0$ represents the O′ phase, and $|\eta_p| > 0.2$ and $\varphi_p > 0$ represents the α″ phase. The positive and negative value for η_p denotes two opposite shuffle directions within the same shuffle plane. As for the shuffle-regulated β → α″ transformation, i.e., under the condition that one of the twelve $\{011\}\langle 0\bar{1}1\rangle_{\beta}$ shuffle goes first, the $\{2\bar{1}1\}\langle\bar{1}\bar{1}1\rangle_{\beta}$ shear will be reduced from 12 possible shear modes to 2. For example [34], when the $(011)[0\bar{1}1]_{\beta}$ shuffle goes first, only $(2\bar{1}1)[1\bar{1}1]_{\beta}$ and $(21\bar{1})[\bar{1}1\bar{1}]_{\beta}$ shear can occur to form the α″ (orthorhombic) phase since the other shear modes such as $(211)[\bar{1}11]_{\beta}$ will make the shuffle atoms out of the $(011)_{\beta}$ plane and the initial bcc lattice will transform to the monoclinic structure.

The degree of shuffle at the energy-minimum state at different Nb concentrations, $\eta_0(x_{Nb})$, which can be obtained from the first-principles calculations (Fig. 5(a)):

$$\eta_0(x_{Nb}) = \begin{cases} 0.98942 - 0.02642 \times x_{Nb}, & 15\ \text{at.\%} \le x_{Nb} \le 37\ \text{at.\%} \\ 0, & x_{Nb} > 37\ \text{at.\%} \end{cases} \tag{16}$$

Moreover, $\eta_0(x_{Nb})$ is also the equilibrium value of shuffle in the phase field model at 0 K and is the analytical solution of Eq. (9):

$$\frac{\partial f_{ch}}{\partial \eta}|_{T=0K} = \eta_0\left(A_1^0(0-T^0) - A_2(\eta_0)^2 + A_3(\eta_0)^4\right) = 0,\ \ \eta_0 \ge 0 \tag{17}$$

Both the β → O′ transition temperature (O_s) and the β → α″ transition temperature (α_s) are concentration dependent, as shown in Fig. 5(d). Experimental reported β → α″ transformation temperature (i.e., α_s, in our current work) in Ti-Nb binary alloys [20–24] shows a continuous decrease with increasing Nb concentration, which has been used to fit the α_s in our simulations. The expansion coefficient $A_1 = A_1^0(T - T^0(x_{Nb}))$ in our phase field simulations in Eq. (9) depends on temperature and Nb concentration, A_1^0 is a positive constant, T is the absolute temperature, and $T^0(x_{Nb})$ is the critical transition temperature derived from M_s (i.e., α_s, in our current work) in Ti-Nb binary alloys [20–24]:

$$T^0(x_{Nb}) = \begin{cases} 1240 - 37 \times x_{Nb}\ \text{K}, & 20\ \text{at.\%} \le x_{Nb} < 25\ \text{at.\%} \\ 1050 - 15 \times x_{Nb}\ \text{K}, & x_{Nb} \ge 25\ \text{at.\%} \end{cases} \tag{18}$$

The expansion coefficient A_2 in Eq. (9) can be extrapolated from Eq. (17):

$$A_2 = \frac{A_3 \cdot (\eta_0)^4 + A_1^0(0 - T^0)}{(\eta_0)^2} \tag{19}$$

In our current work, constants $A_1^0 = 0.001$ and expansion coefficient $A_3 = 37.5$ are used in the phase field model, then substituting η_0 and T^0 in

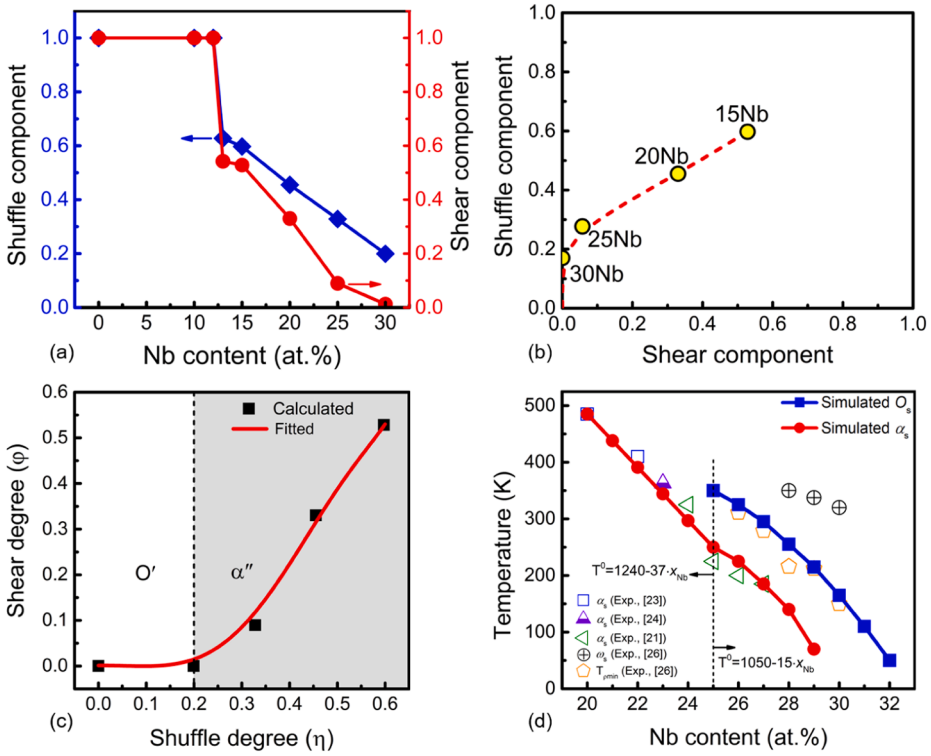

Fig. 5. (a) The shuffle and shear components corresponding to the energy-minimum state as a function of Nb content. (b) A fitted dashed curve based on four Ti-*x*Nb positions and beta position, showing the coupling relationship between the shuffle and shear components for the β → α″ transformation. (c) The unified shear-shuffle relationship used in our phase field model based on (a, b). (d) The available experimental results (Kim et al. [23], Tahara et al. [24], Wang et al. [21] and Todai et al. [26]) for α_s, ω_s and $T_{\rho min}$. Fitted O_s and α_s as a function of Nb content in our simulations.

Eq. (19) by x_{Nb}, we obtain the concentration-dependent A_2, and can be fitted as:

$$A_2(x_{Nb}) = 76649.44755 - 28543.23171x_{Nb} + 4598.89651x_{Nb}^2 - 418.5462x_{Nb}^3 + 23.52946x_{Nb}^4 - 0.83663x_{Nb}^5 + 0.01837x_{Nb}^6 - (2.2794\text{E}-4)x_{Nb}^7 + (1.22294\text{E}-6)x_{Nb}^8 \quad (20)$$

The expansion coefficient A_2 in Eq. (20) continuously decreases from positive value (e.g., A_2= 11.22 for Ti-15 at.% Nb and A_2= 5.57 for Ti-20 at.% Nb) to negative value (e.g., A_2= −2.18 for Ti-25 at.% Nb and A_2= −14.04 for Ti-30 at.% Nb) with Nb increasing, which causes the sharp transition from normal β → α″ at low Nb concentration (x_{Nb} < 25 at.%) to continuous β → O′ → α″ transformations at higher Nb concentration (x_{Nb} ≥ 25 at.%). As a result, the simulated α_s is obtained and is consistent with the experimental α_s, and the O_s is also simulated and marked by blue squares which seems consistent with the temperature with minimum electrical resistivity, $T_{\rho min}$ [26]. Simultaneously, the athermal ω phase transition temperatures (ω_s) have been exhibited in Fig. 5(d) according to the inflection point in electrical resistivity curves [26], which is higher than the O_s used in our simulations. Note that only one order parameter for shuffle (η) is used to distinguish O′ and α" and describe the entire transition in our simulations. The shear (φ) is assumed to be a function of shuffle (not an independent variable anymore) as shown in Eq. (15). This is equivalent to substituting the equilibrium shear order parameter as a function of the shuffle order parameter (obtained by the first principle calculations at 0 K) into the free energy, then the free energy could be presented as a function of the shuffle order parameter only.

3.4. Microstructural evolution upon cooling

Based on the concentration field developed after water quenching in Fig. 2(a, b) and the relationship between the degrees of shear (φ) and shuffle (η) in Fig. 5(c), phase field simulations are carried out to reveal the phase transformation behavior and microstructural evolution as a function of temperature. A continuous transformation is observed in the compositionally modulated Ti-50 at.% Nb system with Nb lean region (25 at.% − 32 at.% Nb) and Nb rich region (55 at.% − 70 at.% Nb) during cooling and heating, which generates randomly distributed nanodomains of O′ and α″ in β matrix, as shown in Fig. 6. Fig. 6(a) shows the appearance of O′ and α″ nanodomains produced by continuous formation and growth upon cooling, and continuous disappearance upon heating. The formation of nanodomains is driven by the Langevin noise term which depends on the temperature as shown in Eq. (14). The shuffle domains (O′) form first followed by the formation of the shear domains (α″) upon further cooling. Morphologically, the equilibrium shape of the O′ nanodomains would be spherical and ignoring coherency strain since the shear (φ) is 0 for the β → O′ transformation. Notably, the O′ nanodomains provide precursors for the formation of the α″ nanodomains, but only certain α″ variants can form. For example, Fig. 7 has shown that the nuclei of the α″ phase form firstly in the interior of the O′ domains. Such nanodomain morphology is distinctively different from that of normal MT [77,78] showing internally-twinned martensitic plates, and the continuous transformation behavior within a broad temperature range is in sharp contrast to the sharp transition in a narrow temperature range of normal MTs.

The characteristics of nanodomain formation are further examined by considering the volume fraction transformed, storage modulus, and internal friction. The volume fractions of the shuffle (O′) and shear (α″) domains are shown in Fig. 6(b), which demonstrate that both the shuffle and shear domains increase or decrease gradually and continuously upon cooling and heating within a broad temperature range. The transition temperatures for the shuffle and shear domains are the same as the transition temperatures of Ti-25 at.% Nb, i.e., O_s and α_s, are ~350 K and ~250 K, respectively, since the leanest Nb-lean region of the WQ sample is ~25 at.% Nb (Fig. 2). The temperature-dependence of the calculated storage modulus and internal friction curves are shown in Fig. 6(c), which reveal the characteristics of a strain glass transition, i.e., exhibiting a frequency dispersion around T_g, which follows the Vogel-Fulcher relation with T_0=130 K, and is consistent with the experimental observations in TiNb-based β-Ti alloys that show strain glass transitions [21, 34].

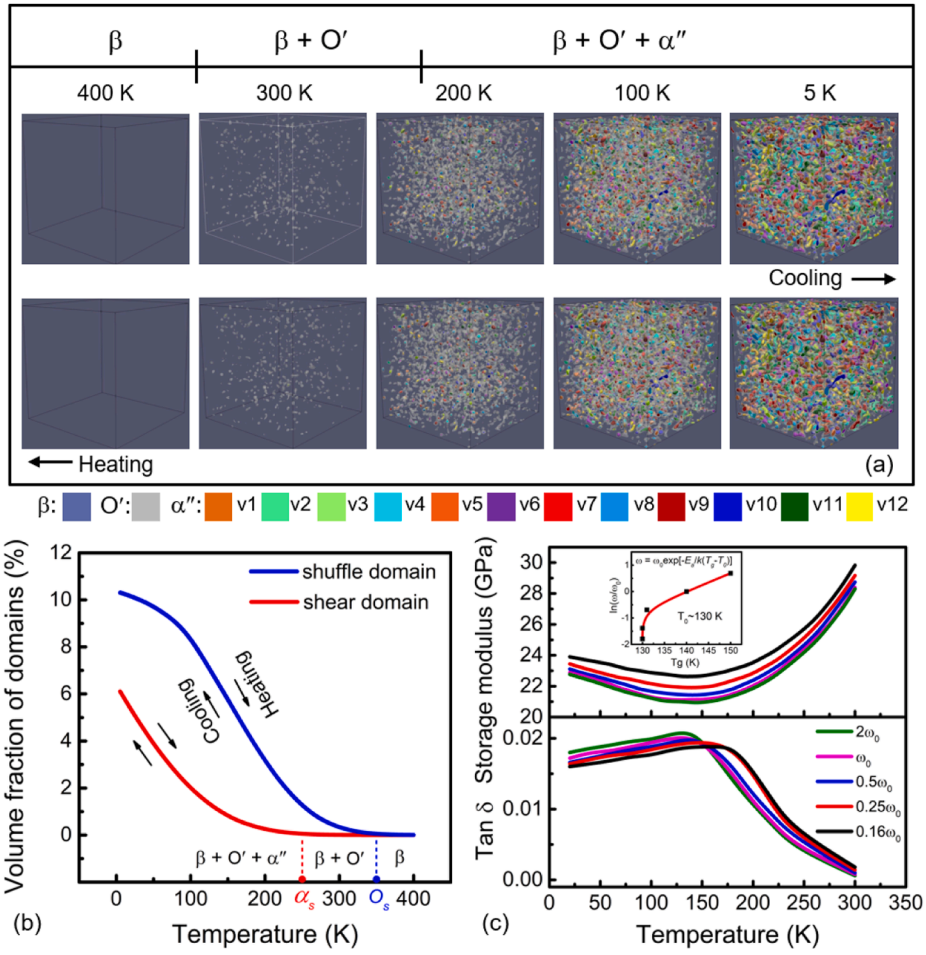

Fig. 6. Transformation characteristics of the compositionally modulated Ti-50 at.% Nb system upon cooling and heating. (a) Calculated microstructural evolution upon cooling and heating, where the β matrix is represented by blue gray, the O′ phase is represented by translucent pale, and the 12 variants of the α″ phase are presented in different colors. (b) Changes in volume fractions of the shuffle and shear domains upon cooling and heating. (c) Temperature-dependence of the storage modulus and internal friction curves. The inset shows the Vogel-Fulcher relation between frequency and T_g.

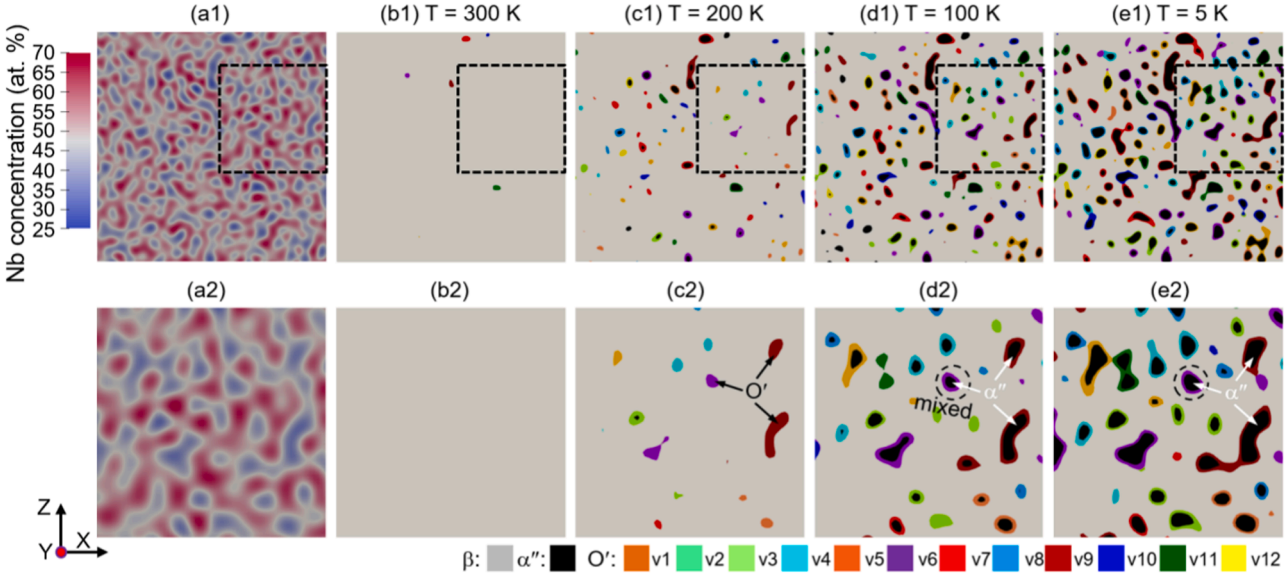

Fig. 7. (a1) 2D cross-sections of the 3D microstructures shown in Fig. 6(a). (a1) Nb concentration field with modulations of solute-lean and solute-rich regions. (b1-e1) Microstructural evolution of nanodomains during cooling. (a2-e2) are zoom-in of the dashed box in (a1-e1).

In order to illustrate the relationship between the spatial variation of Nb concentration and the formation sequence of different nanodomains, the microstructural evolution upon cooling is further analyzed in 2D cross sections as shown in Fig. 7(a1–e1). According to above assumptions, the Nb lean regions (25 at.% – 27 at.%) will transform into O' and the other regions (> 27 at.%) will remain as β phase at room temperature. Enlarged microstructural details of local regions within the black dash squares are presented in Fig. 7(a2–e2). It can be readily seen

that upon cooling, nanodomains of different variants of O′ (marked by the black arrows in Fig. 7(c2)) form first and then nanodomains of α″ (marked by the white arrows in Fig. 7(d2)) form within the O′ domains. Such a nanodomain structure of the martensitic phase is the typical microstructural feature of strain glasses [79]. The O′ nanodomains form within the Nb-lean regions and grow toward the Nb-rich regions upon cooling, while the α″ nanodomains form at the centers of the O′ nanodomains and grow towards the edges (see the white arrows in Fig. 7 (e2)). The Nb concentration range within which the O′ and α″ nanodomains can form upon cooling is about 25 at.% – 32 at.% Nb and 25 at.% – 29.5 at.% Nb, respectively. Note that there is no formation of α″ nanodomains directly from the β matrix in such a concentration modulation system. Experimentally, the $\{011\}\langle 0\bar{1}1\rangle_{\beta}$ type shuffle and related nanodomain structures were observed before the formation of α″ martensite in Ti-23Nb-1.0O alloy using *in-situ* tensile XRD analysis and TEM characterization [24], and the nanodomain density decreases with increasing Nb content in Ti-Nb-Zr-Ta-O alloys [11]. Our calculations thus conclude that the O′ nanodomains prefer to form at the Nb-lean regions and regulate the subsequent formation of α″ nanodomains.

Morphologically, all the α″ nanodomains exist in the interior of existing O′ nanodomains, leading to core-shell structures as shown in Fig. 7(d2, e2). The core-shell structures imply a continuous change in the degree of shuffle (η) across the boundaries. Thus, it is crucial to verify the possibility of the formation of such core-shell nanodomain structures. The related experiments have been done by carrying out the measurements from HAADF-STEM images, which will be described in the next section.

3.5. Experimentally-observed shuffle nanodomains

To confirm our calculations, experimental characterization has been carried out to study changes in the shuffle and shear components across a single nanodomain [34,40] as shown in Fig. 8. The shuffle and shear components have been quantified by analyzing the HAADF-STEM images in Fig. 8, and their definitions are the same as those given in the first-principles calculations (Section 3.2). The lattice structure of the nanodomains at room temperature is characterized from $[110]_{\beta}$ zone axis, respectively, showing single O′ and α″ nanodomains as highlighted by the blue and red circles in Fig. 8(a) and (e), respectively. The O′ in Fig. 8(a–d) is detected in solution-treated Ti2448, while the α″ in Fig. 8 (e–h) is detected in 50% cold-rolled Ti2448 after solution treatment. In our observations, every other $(110)_{\beta}$ plane shuffle along the $[1\bar{1}0]_{\beta}$ direction in Fig. 8(a) and (e). The two shuffles are further validated by the line intensity profiles (Fig. 8(c, g)) plotted along the yellow lines across the non-shuffled and shuffled atomic columns in Fig. 8(a, e), respectively. The shuffle components of the O′ and α″ domains are then evaluated by direct measurements of the displacements of atomic columns on every other plane $(110)_{\beta}$ along the shuffle direction $[1\bar{1}0]_{\beta}$. The distance of the atomic shuffle has been defined to be $z=(x-y)/2$, as shown in Figs. 3 and 8(a, e), and can be quantified using the difference of the atomic column intensity peak locations that are exampled in Fig. 8(b, f).

Three features should be noted about the shuffle and shear components (Fig. 8(d, h)). First, the shuffle components are larger than the shear components in both the O′ and α″ nanodomains. Second, both the shuffle and shear components of the α″ domain are significantly larger

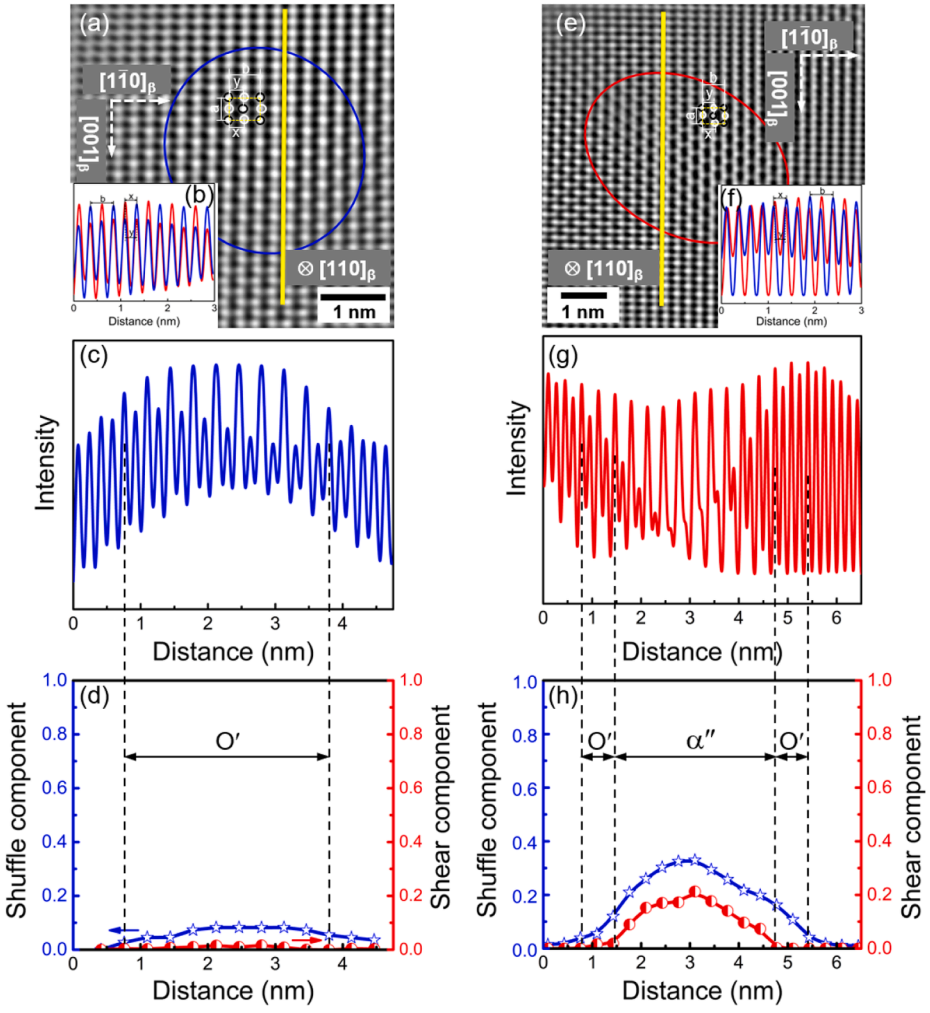

Fig. 8. HAADF-STEM images showing orthorhombic nanodomains in Ti2448 at room temperature. (a, e) HAADF-STEM images recorded with the incident beam parallel to $[110]_{\beta}$, showing single O′ and α″ nanodomains marked by the blue and red color circles, respectively. The O′ nanodomain is detected in solution-treated Ti2448, while the α″ nanodomain is detected in 50% cold-rolled Ti2448 after solution treatment. (b, f) Two examples about the corresponding intensity profiles along the shuffle directions in the O′ and α″ nanodomains, showing the displacement of every other shuffle plane. (c, g) Intensity profiles along the yellow lines in (a) and (e), respectively. (d, h) Calculated shuffle and shear components along the yellow lines in (a) and (e), respectively. (For interpretation of the references to color in this figure legend, readers are referred to the web version of this article.)

than that of the O′ domain and the shear component of the O′ domain is almost zero. This is consistent with the intensity profiles shown in Fig. 8 (c) and 8(g) where the intensity difference between every other $(110)_\beta$ plane along the $[1\bar{1}0]_\beta$ direction in the α″ variant (Fig. 8(g)) is more pronounced than the intensity difference in the O′ variant (Fig. 8(c)). Third, continuous changes of the shuffle components across the boundaries can be found in the non-shuffled and shuffled atomic columns. The shuffle component continuously increases at the boundaries from the matrix to the nanodomain region (O′ to α″) as shown in Fig. 8 (d, h), and no sharp interfaces have been detected, which confirms the existence of continuous β → O′ → α″ transition. Especially, the continuously-increased shuffle component from the outside into the interior of the α″ nanodomain in Fig. 8(g) confirms the possibility of the core-shell structure obtained from the calculations in Fig. 7.

4. Discussion

4.1. Continuous change of the shuffle degree upon cooling

The above simulations and experimental observations have shown the existence of O′ nanodomains at high temperature and α″ nanodomains at low temperature, suggesting a continuous β → O′ → α″ transformation. This transformation behavior is accompanied by a unique core-shell nanodomain structure over a wide temperature range (Figs. 6 and 7). To understand this particular phase transformation path, the temperature dependence of the order parameter has been calculated and analyzed. The enlarged microstructures from Fig. 6(a) and the related 1D profiles for the order parameters along the body-diagonal of $8l_o \times 8l_o \times 8l_o$ grids are shown in Fig. 9, which contains a single nanodomain located in the center of the computational cell. Fig. 9(a) shows the continuous formation and growth of the O′ and α″ nanodomains. The α″ nanodomain appears in the O′ domain with the formation of core-shell structure, suggesting a shuffle-domain regulated α″ nanodomain mechanism. Two locations of interest have been marked by point 5 (yellow dot) in the center of the nanodomain and point 6 (turquoise dot) in the boundary of the nanodomain. Fig. 9(c) shows the line profiles of the shuffle degree (η) upon cooling, indicating a significant increase in the degree of shuffle as well as in domain size upon cooling. In addition, the shuffle degree (η) vs. temperature plots at points 5 and 6 are shown in Fig. 9(d), which also exhibit a continuous increase in the degrees of shuffle upon cooling. The continuous increase of the shuffle degree (η) results in a continuous increase of the shear degree (φ) according to Eq. (15) and as shown in Fig. 9(e). Moreover, the volume of the nanodomains in the $8l_o \times 8l_o \times 8l_o$ computational cells is shown in Fig. 9(b), which shows that the local transition temperatures for the O′ and α″ can be determined to be 300 K and 250 K, respectively, in this region. Note that the formation temperatures of the O′ and α″ nanodomains at local regions are different from the overall (average) transition temperatures of the Ti-Nb system (Fig. 6) due to the inhomogeneity of Nb concentration. Because of spinodal decomposition, concentration gradients will be present during water quenching and the center of the O′ domain will have the lowest Nb concentration, implying the highest transformation temperature (for both O′ and α″). The lower transition temperature for the formation of α″ results in the formation of core-shear structure and shuffle regulated α″ phase.

Both the shuffle and shear degrees during the β → α″ transformation in the local regions increase continuously upon cooling, resembling a high-order transitions (rather than a first-order transition). Similarly, previous works have also shown continuous atomic arrangements for phase transformations in concentration-modulated TiNb-based alloys [4,17,18,39]. For example, a continuous transformation from bcc to hcp keeping orthorhombic symmetry was found in Ti2448 by *in-situ* SXRD analysis from 648 K to 848 K [17], which can be attributed mainly to the continuous increase of atomic shuffle and shear in the Nb-lean regions produced by spinodal decomposition. A similarly continuous but reversible increase of shuffle and shear has also been found in Nb-lean regions of Ti2448 by *in-situ* tensile SXRD profiles from 0 to 600 MPa [4,18]. Especially, a continuous increase of normal strain $\varepsilon_x(x\ //\ [011]_\beta)$

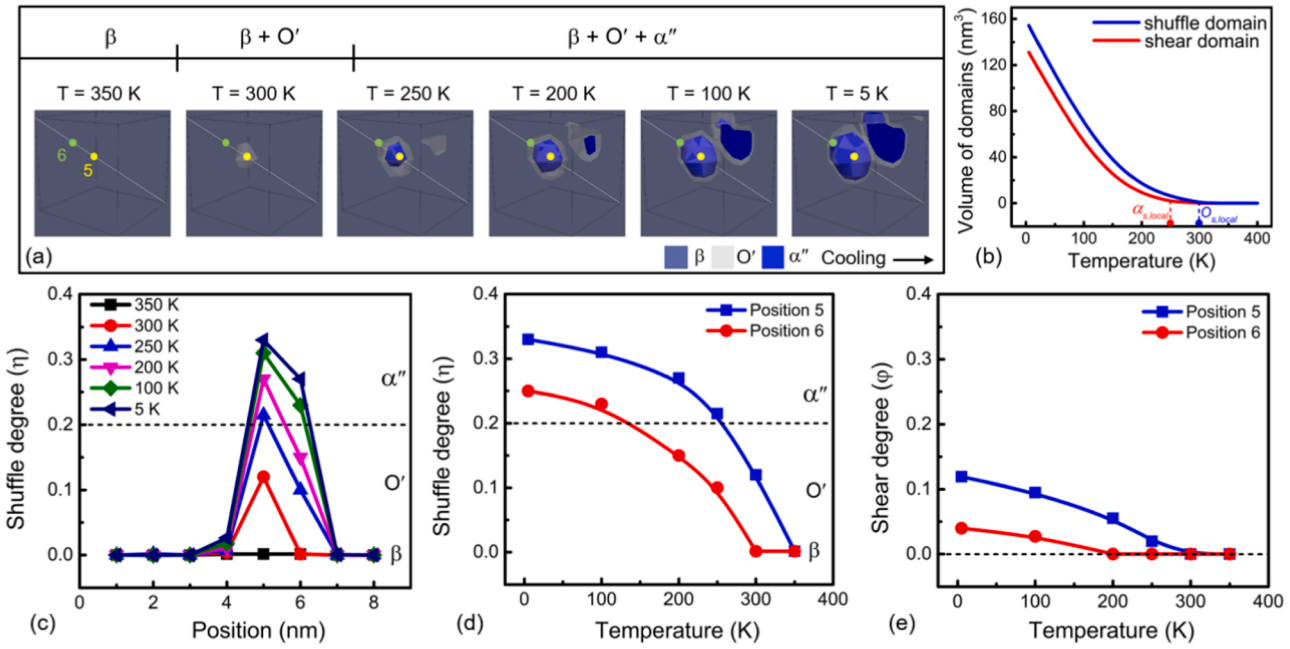

Fig. 9. Enlarged images of Fig. 6(a) showing continuous β → O′ → α″ transformation upon cooling in a $8l_o \times 8l_o \times 8l_o$ local volume element. (a) Microstructural evolution, where the β matrix is represented by blue gray, the O′ variant is represented by translucent pale and the 10th variant of the α″ is represented by blue. (b) Changes in the volume of the nanodomains upon cooling in the $8l_o \times 8l_o \times 8l_o$ computational cells. (c) 1D shuffle degree (η) profiles along the body-diagonal of the computational cells. (d, e) Evolution of the shuffle degree (η) and the corresponding shear degree (φ) upon cooling at positions 5 and 6 indicated by the yellow and turquoise dots in (a). (For interpretation of the references to color in this figure legend, readers are referred to the web version of this article.)

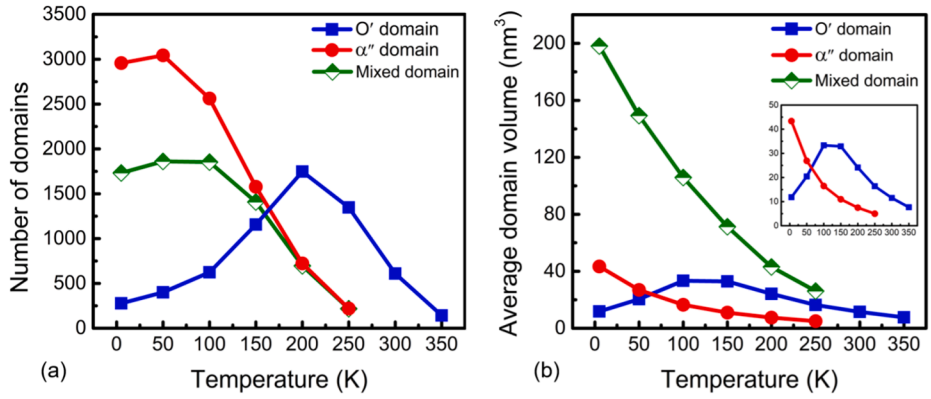

Fig. 10. Quantitative analysis of microstructural evolution shown in Fig. 6, revealing nanodomain formation and growth upon cooling. (a) Calculated domain numbers of the O′, α″ and mixed core-shell nanodomains as a function of temperature. (b) Calculated average domain volume of the O′, α″ and mixed core-shell nanodomains as a function of temperature.

has also been detected across the interfaces between the β matrix and isothermal α″ (and α) precipitates in aged Ti2448 [39], showing a continuous β → isothermal α″ → α transformation as the aging temperature increases from 673 K to 723 K.

4.2. Characteristics of the nanodomain structures

In addition to the continuous increase of shuffle (η) and shear (φ) in a single nanodomain upon cooling, the microstructure evolution of the whole system is characterized by the formation of high density nanodomains with limited growth upon cooling. Based on the results shown in Figs. 6 and 7, the shuffle and shear domains can be further divided into three domain structures: individual O′ domains, individual α″ domains and mixed core-shell domains. Fig. 10 shows the number density and average volume of these nanodomains as a function of temperature. A significant amount of O′ domains appear at about 350 K and continue to increase and peak at 200 K. The α″ domains start to form within some of the existing O′ domains at 250 K, leading to mixed core-shell domains.

The average volume of the α″ and the mixed domains continuously increase but that of the O′ domain first increases ($T \geq 100$ K) and then decreases ($T < 100$ K) upon further cooling, which indicates that the Nb-lean regions (β) continue to transform to O′ and the O′ phase gradually transform to α″ upon cooling. Thus, the number of α″ domains shows a maximum value at lower temperature (50 K) than that of O′ domains. In addition, we find that some mixed domains can interconnect into one mixed domain at lower temperature (Fig. 7), and the mixed domain has maximum average volume at low temperature, indicating that the increased driving force by cooling for domain growth is easier than that for nucleation of new domains, being accordance with that of strain glass transition with accelerating kinetics upon cooling [80].

Such a continuous increase of area fraction and the average size of nanodomains has been observed in solution-treated Ti2448 via *in-situ* cooling TEM characterization [34], which is different from conventional MT with rapid growth after nucleation in binary Ti-(20–24 at.%) Nb [72,78]. The continuous strain glass transition has been attributed to the existence of local stress field caused by point defects [77,81], nano-precipitates [82], or other structural disturbances [83]. It has also been shown [15,47,84] that nanoscale concentration modulations are also effective to make the MTs apparently continuous in Ti2448 by considering the Nb-concentration dependence of the temperature. By considering the shuffle degree in this study, the formation and limited growth of nanosized domains can be understood: the limited growth of the shuffle domains is inhibited upon cooling by the intrinsically smaller composition inhomogeneity obtained by spinodal decomposition and the shuffle domain regulated the further growth of α″ at lower temperature. The current study suggests that the concentration modulation-induced shuffle domains may have played an important role in making the MT continuous in Ti2448.

4.3. Physical origin of superelasticity over a wide temperature range

Experiments have shown superelasticity (SE) over wide temperature ranges in TiNb-based alloys [5,13], which have been explained by randomly distributed α″ martensite nanodomains due to the existence of interstitial oxygen. However, this mechanism may not explain the similar SE observed in Ti2448 without oxygen doping [3]. To understand SE over a wide temperature range [3], the stress-strain curves of the compositionally modulated Ti-50 at.% Nb system have been

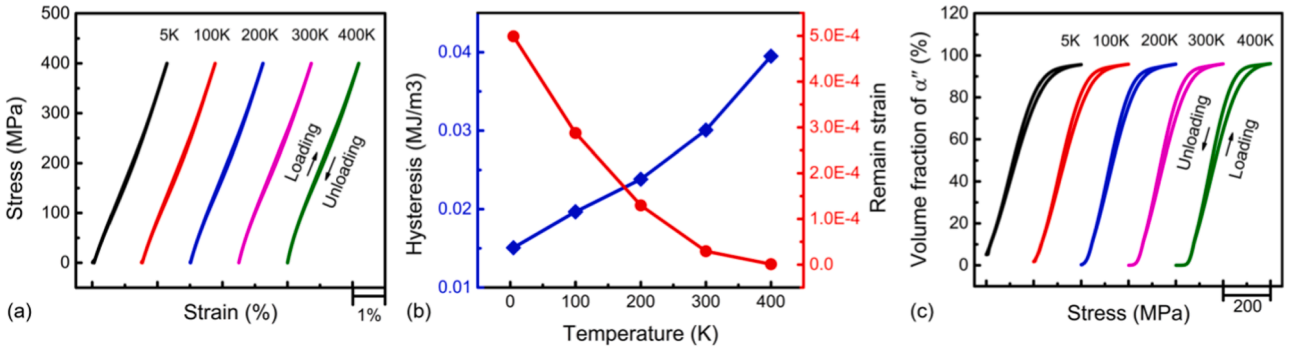

Fig. 11. Mechanical properties and evolution of volume fraction of the α″ phase in a compositionally modulated Ti-50 at.% Nb system at different temperatures. (a) Stress-strain curves obtained from the first loading-unloading cycle. (b) The hysteresis area and residual strain obtained from the stress-strain curves of (a). (c) The volume fraction of the stress-induced α″ martensite during the first cyclic loading of the computation cells.

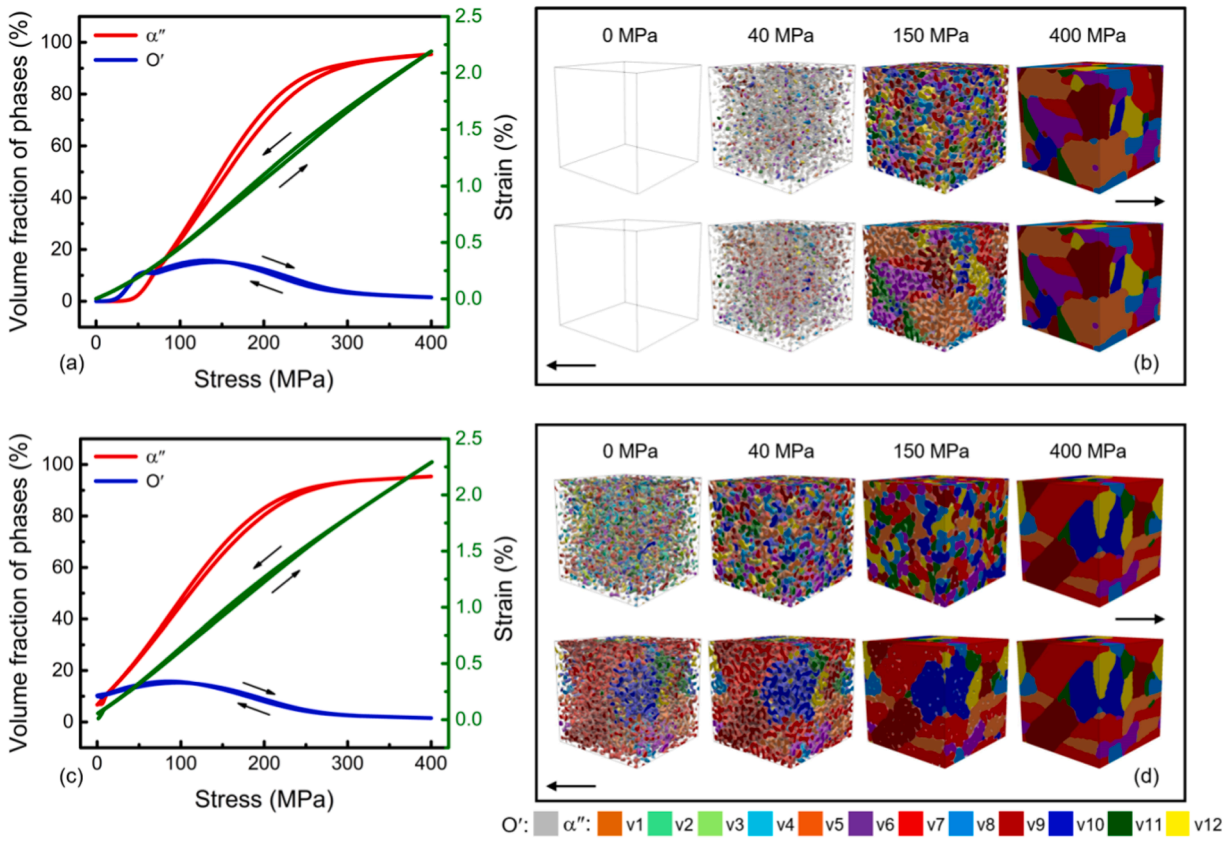

Fig. 12. Microstructural evolution in the compositionally modulated Ti-50 at.% Nb system during the first loading and unloading at 400 K and 5 K. (a, c) Volume fraction of the O′ and α″ phases and strain-stress curves at 400 K and 5 K respectively. (b, d) Microstructural evolution in the computational cells at 400 K and 5 K respectively, where the parent β phase is set transparent, the O′ is represented by translucent pale and different variants (v1-v12) of the α″ are plotted as iso-surfaces with different colors, as indicated in the color map at the bottom.

simulated during the first loading-unloading cycle at the temperature range of 5 and 400 K as shown in Fig. 11. A tensile stress along the $[100]_{\beta}$ direction is applied, which prefers α″ phase with the 5th-12th variants. The Ti-50 at.% Nb system with concentration modulations due to solution treatment plus water quench has shown linear SE with near-zero hysteresis, and small residual strain over a wide temperature range (5–400 K), being consistent with the experimental observations in Ti2448 [3]. The operating temperature range for SE is wider than that of traditional NiTi SMAs [77,85] and Fe-bases SMAs [86,87]. In addition, linear stress-stain behavior has also been reported in pre-strained TiNb-based systems [15], in which the continuous growth of retained α″ martensite can be the origin. Moreover, NiTi SMAs with nanoscale concentration gradient also presented linear SE [88]. In our case, the nanoscale concentration modulations caused by spinodal decomposition could limit the growth of O′ nanodomains and the pre-formed shuffle domains may regulate the formation of sheared α″, bringing a continuous transition of β → O′ → α″. This continuously-changed shuffle and shear and limited domain size upon cooling may lead to the quasi-linear

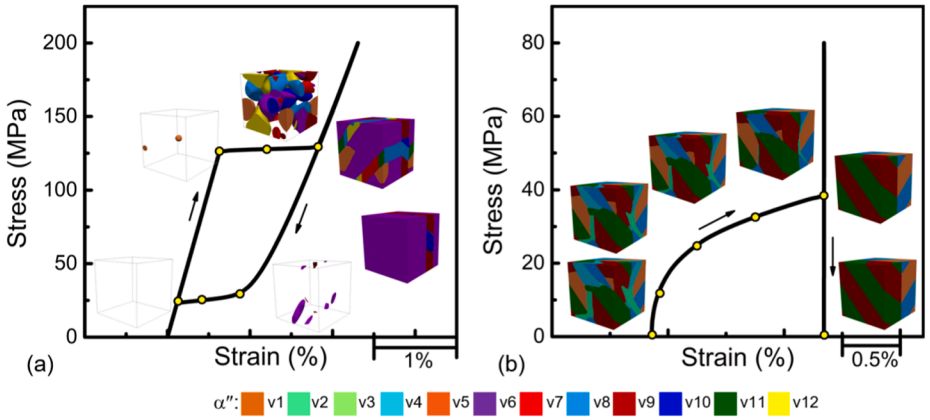

Fig. 13. Calculated stress-strain curves and the corresponding microstructural evolution in a system with a uniform Nb concentration of Ti-20 at.% Nb at (a) $T = 650$ K ($>A_f$ ~560 K) and (b) $T = 400$ K ($<M_s$ ~485 K). The parent phase is transparent and the martensitic variants are various colors.

SE over a wide temperature range.

Being consistent with the variation of stress-strain curves, the volume fraction of the stress-induced α″ shows a continuous change as a function of stress at different temperatures (Fig. 11(c)). The continuous increase of the volume fraction of α″ is the cause of the quasi-linear SE. Related microstructural evolution under different loading conditions is shown in Figs. 12-13. Fig. 12 shows the microstructural evolution as a function of stress for the compositionally modulated Ti-50 at.% Nb system at 400 K and 5 K. The results indicate that the external load favors the formation of α″ phase. At 400 K (Fig. 12(a, b)), the β phase (transparent) is the stable phase, and two stages of phase transformation can be identified upon loading. In the current phase field model for improper MT, the strain ε_{kl}^{MT} is coupled to the primary order parameter [89], shuffle η, and $\varepsilon_{kl}^{MT} = \sum_{p=1}^{6} \varepsilon_{kl}^{0}(p)\varphi_p$ can be further expressed based on the relationship between the shear (φ) and shuffle (η) in Eq. (15). Thus, the intermediate O′ nanodomains are inevitably formed upon loading in the compositionally modulated Ti-50 at.% Nb system. At low stress level of σ<50 MPa, the O′ nanodomains appear firstly then transform to α″ nanodomains. But when σ>50 MPa, the nanodomains gradually transform to the long-range ordered α″ martensite with ~95% volume fraction at the end of loading. As for the morphology of long-range ordered α″, relatively flat twin boundaries exist between the variants of α″ with different shear modes, but curved boundaries are found between the variants of α″ with the same shear mode but different shuffle modes. Our simulations are consistent with the experimental observations in TiNbO alloys [13], which indicated stress induced transition from strain glass state to martensite. During unloading, a reverse process can be detected. At low temperature $T = 5$ K, the α″ phase is the stable phase, the system before loading shows the coexistence of both O′, α″ and mixed nanodomains (Figs. 6 and 7). Under loading, the O′ nanodomains increase firstly then decrease but the α″ nanodomains increase continuously, the system will transform into a twinned martensitic state. In contrast, Fig. 13 shows the stress-strain curves and the corresponding microstructural evolution for normal MT in Ti-20 at.% Nb at 650 K ($>A_f$ ~560 K) and 400 K ($<M_s$ ~485 K) respectively. SE with large hysteresis is observed at 650 K (Fig. 13(a)). A critical applied load is needed to trigger the nucleation of α″ martensite upon loading and the nucleation of β phase upon unloading, resulting in a large hysteresis. The curved boundaries are also found between the variants (such as v9-v10) of the stress-induced α″ with the same shear mode but opposite shuffle directions. At $T = 400$ K, a detwinning process with large hysteresis and remnant strain is obtained (Fig. 13(b)), accompanied by non-recoverable strain.

5. Conclusion

In summary, we have revealed the mechanism of shuffle-regulated strain glass transition of β → O′ → α″ in Ti-Nb-based SMAs by integrating thermodynamic database, first-principles calculations, phase field simulations and experiments. Concentration modulations with ~10 nm wavelength are generated by spinodal decomposition. Total energies of the β→ α″ transformation for four Ti-Nb binary systems are calculated by first principles as a function of the shear and shuffle components, showing the change of phase transformation path from β → α″ to β → O′ with increasing Nb content. Both the shuffle and shear components show concentration dependence, i.e., decreasing with increasing Nb content, and can be coupled together. Phase field simulations that consider the coupling between the concentration modulations and the shear-shuffle modes of the transformations demonstrate that concentration modulations caused by spinodal decomposition create local concentration field that induces O′ nanodomains formation at the Nb-lean regions, then the continuously-increased shear induces the formation of α″ nanodomains. The α″ nanodomains form in the interior of the formed O′ nanodomains, which lead to the mixed nanodomains. This core-shell structure has been proved by our experimental observations. The concentration field limits the growth of both O′ and α″ nanodomain size and could be the origin of continuous transition. As a result, a synergistic combination of linear superelasticity, almost zero hysteresis and remnant strain across a wide temperature range is achieved.

Declaration of Competing Interest

The authors declare that they have no known competing financial interests or personal relationships that could have appeared to influence the work reported in this paper.

Acknowledgments

The authors would like to acknowledge fruitful discussions with Prof. Liang Qi from University of Michigan. DW would like to acknowledge the support from the National Key Research and Development Program of China (Grand No. 2021YFB3702603), the National Natural Science Foundation of China (Grants No. 51931004 and 52171012), the Fundamental Research Funds for the Central Universities (xhj032021015-06) and 111 project (BP2018008). HZ acknowledges the support of the National Natural Science Foundation of China (Grants No. 51871175). YZ appreciates the financial support from the faculty startup funding from University of Nevada, Reno. YW acknowledges the support of the US National Science Foundation (Grant DMR-1923929), which has facilitated this international collaboration.

References

[1] A. Biesiekieski, J. Wang, M. Abdel-Hady Gepreel, C. Wen, A new look at biomedical Ti-based shape memory alloys, Acta Biomater. 8 (2012) 1661–1669.
[2] M. Niinomi, M. Nakai, J. Hieda, Development of new metallic alloys for biomedical applications, Acta Biomater. 8 (2012) 3888–3903.
[3] H. Wang, Y. Hao, S. He, T. Li, J.M. Cairney, Y. Wang, Y. Wang, E.G. Obbard, F. Prima, K. Du, S. Li, R. Yang, Elastically confined martensitic transformation at the nano-scale in a multifunctional titanium alloy, Acta Mater. 135 (2017) 330–339.
[4] Y. Hao, H. Wang, T. Li, J.M. Cairney, A.V. Ceguerra, Y. Wang, Y. Wang, D. Wang, E. G. Obbard, S. Li, R. Yang, Superelasticity and tunable thermal expansion across a wide temperature range, J. Mater. Sci. Technol. 32 (2016) 705–709.
[5] L. Wei, H.Y. Kim, T. Koyano, S. Miyazaki, Effects of oxygen concentration and temperature on deformation behavior of Ti-Nb-Zr-Ta-O alloys, Scr. Mater. 123 (2016) 55–58.
[6] Y. Hao, S. Li, F. Prima, R. Yang, Controlling reversible martensitic transformation in titanium alloys with high strength and low modulus, Scr. Mater. 67 (2012) 487–490.
[7] Y. Zhang, S. Li, E.G. Obbard, H. Wang, S. Wang, Y. Hao, R. Yang, Elastic properties of Ti-24Nb-4Zr-8Sn single crystals with bcc crystal structure, Acta Mater. 59 (2011) 3081–3090.
[8] Y. Hao, S. Li, B. Sun, M. Sui, R. Yang, Ductile titanium alloy with low poisson's ratio, Phys. Rev. Lett. 98 (2007), 216405.
[9] D.L. Gong, H.L. Wang, E.G. Obbard, S.J. Li, R. Yang, Y.L. Hao, Tuning thermal expansion by a continuing atomic rearrangement mechanism in a multifunctional titanium alloy, J. Mater. Sci. Technol. 80 (2021) 234–243.
[10] H.Y. Kim, L. Wei, S. Kobayashi, M. Tahara, S. Miyazaki, Nanodomain structure and its effect on abnormal thermal expansion behavior of a Ti-23Nb-2Zr-0.7Ta-1.2O alloy, Acta Mater. 61 (2013) 4874–4886.
[11] L. Wei, H.Y. Kim, S. Miyazaki, Effects of oxygen concentration and phase stability on nano-domain structure and thermal expansion behavior of Ti-Nb-Zr-Ta-O alloys, Acta Mater. 100 (2015) 313–322.
[12] J. Fu, A. Yamamoto, H.Y. Kim, H. Hosoda, S. Miyazaki, Novel Ti-base superelastic alloys with large recovery strain and excellent biocompatibility, Acta Biomater. 17 (2015) 56–67.
[13] Y. Nii, T. Arima, H.Y. Kim, S. Miyazaki, Effect of randomness on ferroelastic transitions: disorder-induced hysteresis loop rounding in Ti-Nb-O martensitic alloy, Phys. Rev. B 82 (2010), 214104.
[14] J.P. Liu, Y.D. Wang, Y.L. Hao, Y. Wang, Z.H. Nie, D. Wang, Y. Ren, Z.P. Lu, J. Wang, H. Wang, New intrinsic mechanism on gum-like superelasticity of multifunctional alloys, Sci. Rep. 3 (2013) 2156.
[15] J. Zhu, Y. Gao, D. Wang, J. Li, T.Y. Zhang, Y. Wang, Making metals linear superelastic with ultralow modulus and nearly zero hysteresis, Mater. Horiz. 6 (2019) 515–523.
[16] D. Wang, Q. Liang, S. Zhao, P. Zhao, T. Zhang, L. Cui, Y. Wang, Phase field simulation of martensitic transformation in pre-strained nanocomposite shape memory alloys, Acta Mater. 164 (2019) 99–109.
[17] H. Wang, Y. Hao, S. He, K. Du, E.G. Obbard, J. Hudspeth, J. Wang, Y. Wang, Y. Wang, F. Prima, N. Lu, M.J. Kim, J.M. Cairney, S. Li, R. Yang, Tracing the

coupled atomic shear and shuffle for a cubic to a hexagonal crystal transition, Scr. Mater. 133 (2017) 70–74.
[18] Y.L. Hao, D.L. Gong, H.L. Wang, J.M. Cairney, Y.D. Wang, E.G. Obbard, F. Sun, F. Prima, S.J. Li, K. Du, R. Yang, Continuous and reversible atomic rearrangement in a multifunctional titanium alloy, Materialia 2 (2018) 1–8.
[19] J.P. Liu, Y.D. Wang, Y.L. Hao, H.L. Wang, Y. Wang, Z.H. Nie, R. Su, D. Wang, Y. Ren, Z.P. Lu, High-energy X-ray diffuse scattering studies on deformation-induced spatially confined martensitic transformations in multifunctional Ti-24Nb-4Zr-8Sn alloy, Acta Mater. 81 (2014) 476–486.
[20] M. Bönisch, A. Panigrahi, M. Calin, T. Waitz, M. Zehetbauer, W. Skrotzki, J. Eckert, Thermal stability and latent heat of Nb-rich martensitic Ti-Nb alloys, J. Alloy. Compd. 697 (2017) 300–309.
[21] Y. Wang, J. Gao, H. Wu, S. Yang, X. Ding, D. Wang, X. Ren, Y. Wang, X. Song, J. Gao, Strain glass transition in a multifunctional β-type Ti alloy, Sci. Rep. 4 (2014) 3995.
[22] A.R.G. Brown, D. Clark, J. Eastabrook, K.S. Jepson, The titanium-niobium system, Nature 201 (1964) 914–915.
[23] H.Y. Kim, Y. Ikehara, J.I. Kim, H. Hosoda, S. Miyazaki, Martensitic transformation, shape memory effect and superelasticity of Ti-Nb binary alloys, Acta Mater. 54 (2006) 2419–2429.
[24] M. Tahara, H.Y. Kim, T. Inamura, H. Hosoda, S. Miyazaki, Lattice modulation and superelasticity in oxygen-added β-Ti alloys, Acta Mater. 59 (2011) 6208–6218.
[25] J.Y. Yan, G.B. Olson, Molar volumes of bcc, hcp, and orthorhombic Ti-base solid solutions at room temperature, Calphad 52 (2016) 152–158.
[26] M. Todai, T. Fukuda, T. Kakeshita, Relation between negative temperature coefficient in electrical resistivity and athermal ω phase in Ti-*x*Nb ($26 \leq x \leq 29$ at.%) alloys, J. Alloy. Compd. 577S (2013) S431–S434.
[27] Y. Zheng, R.E.A. Williams, S. Nag, R. Banerjee, H.L. Fraser, D. Banerjee, The effect of alloy composition on instabilities in the β phase of titanium alloys, Scr. Mater. 116 (2016) 49–52.
[28] E.L. Pang, E.J. Pickering, S.I. Baik, N.G. Jones, The effect of zirconium on the omega phase in Ti-24Nb-[0-8]Zr (at.%) alloys, Acta Mater. 153 (2018) 62–70.
[29] T. Li, M. Lai, A. Kostka, S. Salomon, S. Zhang, C. Somsen, M.S. Dargusch, D. Kent, Composition of the nanosized orthorhombic O' phase and its direct transformation to fine α during aging in metastable β-Ti alloys, Scr. Mater. 170 (2019) 183–188.
[30] T. Yano, Y. Murakami, D. Shindo, S. Kuramoto, Study of the nanostructure of Gum Metal using energy-filtered transmission electron microscopy, Acta Mater. 57 (2009) 628–633.
[31] Y. Zheng, D. Banerjee, H.L. Fraser, A nano-scale instability in the β phase of dilute Ti-Mo alloys, Scr. Mater. 116 (2016) 131–134.
[32] Y. Zheng, T. Alam, R. Banerjee, D. Banerjee, H.L. Fraser, The influence of aluminum and oxygen additions on intrinsic structural instabilities in titanium-molybdenum alloys, Scr. Mater. 152 (2018) 150–153.
[33] Y. Zheng, S. Antonov, Q. Feng, R. Banerjee, D. Banerjee, H.L. Fraser, Shuffle-induced modulated structure and heating-induced ordering in the metastable β-titanium alloy, Ti-5Al-5Mo-5V-3Cr, Scr. Mater. 176 (2020) 7–11.
[34] Q. Liang, D. Wang, Y. Zheng, S. Zhao, Y. Gao, Y. Hao, R. Yang, D. Banerjee, H. L. Fraser, Y. Wang, Shuffle-nanodomain regulated strain glass transition in Ti-24Nb-4Zr-8Sn alloy, Acta Mater. 186 (2020) 415–424.
[35] D. Banerjee, K. Murakami, J.L. Strudel, Substructure in titanium alloy martensite, Philos. Mag. A 77 (1998) 299–323.
[36] S. Banerjee, P. Mukhopadhyay, Phase Transformations, Examples from Titanium and Zirconium Alloys, Pergamon, 2007.
[37] Y. Zheng, R. Banerjee, Y. Wang, H. Fraser, D. Banerjee, Pathways to titanium martensite, Trans. Indian Inst. Met. 75 (2022) 1051–1068.
[38] Q. Liang, Y. Zheng, D. Wang, Y. Hao, R. Yang, Y. Wang, H.L. Fraser, Nano-scale structural non-uniformities in gum like Ti-24Nb-4Zr-8Sn metastable β-Ti alloy, Scr. Mater. 158 (2019) 95–99.
[39] L. Qi, S. He, C. Chen, B. Jiang, Y. Hao, H. Ye, R. Yang, K. Du, Difffusional-displacive transformation in a metasble β-titanium alloy and its strengthening effect, Acta Mater. 195 (2020) 151–162.
[40] Q. Liang, Z. Kloenne, Y. Zheng, D. Wang, S. Antonov, Y. Gao, Y. Hao, R. Yang, Y. Wang, H.L. Fraser, The role of nano-scaled structural non-uniformities on deformation twinning and stress-induced transformation in a cold rolled multifunctional β-titanium alloy, Scr. Mater. 177 (2020) 181–185.
[41] D.L. Moffat, U.R. Kattner, The stable and metastable Ti-Nb phase diagrams, Metall. Trans. A 19A (1988) 2389–2397.
[42] Y. Zhang, H. Liu, Z. Jin, Thermodynamic assessment of the Nb-Ti system, Calphad 25 (2001) 305–317.
[43] J.L. Murray, The Mo-Ti (Molybedenum-Titanium) system, Bull. Alloy Phase Diagr. 2 (1981) 185–192.
[44] C. Ghosh, J. Basu, R. Ramachandran, E. Mohandas, Phase separation and ω transformation in binary V-Ti and ternary V-Ti-Cr alloys, Acta Mater. 121 (2016) 310–324.
[45] G. Lindwall, P. Wang, U.R. Kattner, C.E. Campbell, The effect of oxygen on phase equilibria in the Ti-V system: impacts on the AM processing of Ti alloys, JOM 70 (2018) 1692–1705.
[46] Y. Ishiguro, Y. Tsukada, T. Koyama, Phase-field study of the spinodal decomposition rate of β phase in oxygen-added Ti-Nb alloys, Comp. Mater. Sci. 174 (2020), 109471.
[47] J. Zhu, Y. Gao, D. Wang, T.Y. Zhang, Y. Wang, Taming martensitic transformation via concentration modulation at nanoscale, Acta Mater. 130 (2017) 196–207.
[48] W.G. Burgers, On the process of transition of the cubic-body-centered modification into the hexagonal-close-packed modification of zirconium, Physica I (1934) 561–586.
[49] C. Li, H. Luo, Q. Hu, R. Yang, F. Yin, O. Umezawa, L. Vitos, Lattice parameters and relative stability of α'' phase in binary titanium alloys from first-principles calculations, Solid State Commun. 159 (2013) 70–75.
[50] X. Sun, H. Zhang, D. Wang, Q. Sun, S. Zhao, S. Lu, W. Li, L. Vitos, X. Ding, Large recoverable strain with suitable transition temperature in TiNb-based multicomponent shape memory alloys: first-principles calculations, Acta Mater. 221 (2021), 117366.
[51] A.T. Dinsdale, SGTE data for pure elements, Calphad 15 (1991) 317–425.
[52] L. Vitos, Computational Quantum Mechanics For Materials Engineers : The EMTO Method and Applications, Springer-Verlag, London, 2007.
[53] J.P. Perdew, K. Burke, M. Ernzerhof, Generalized gradient approximation made simple, Phys. Rev. Lett. 77 (1996) 3865–3868.
[54] P.A. Korzhavyi, A.V. Ruban, I.A. Abrikosov, H.L. Skriver, Madelung energy for random metallic alloys in the coherent potential approximation, Phys. Rev. B 51 (1995) 5773–5780.
[55] M. Bönisch, A. Panigrahi, M. Stoica, M. Calin, E. Ahrens, M. Zehetbauer, W. Skrotzki, J. Eckert, Giant thermal expansion and α-precipitation pathways in Ti-alloys, Nat. Commun. 8 (2017) 1429.
[56] J. Cahn, J. Hilliard, Free energy of a nonuniform system. I. Interfacial free energy, J. Chem. Phys. 28 (1958) 258–267.
[57] J.S. Langer, M. Bar-On, H.D. Miller, New computational method in the theory of spinodal decomposition, Phys. Rev. A 11 (1975) 1417–1429.
[58] J.W. Cahn, On spinodal decomposition, Acta Metall. 9 (1961) 795–801.
[59] K. Elder, Langevin simulations of nonequilibrium phenomena, Comput. Phys. 7 (1993) 26–33.
[60] P.C. Hohenberg, B.I. Halperin, Theory of dynamic critical phenomena, Rev. Mod. Phys. 49 (1977) 435–479.
[61] T. Helander, J. Agren, A phenomenological treatment of diffusion in Al-Fe and Al-Ni alloys having B2-B.C.C. ordered structure, Acta Mater. 47 (1999) 1141–1152.
[62] J. Wang, H.S. Liu, L.B. Liu, Z.P. Jin, Assessment of diffusion mobilities in FCC Cu-Ni alloys, Calphad 32 (2008) 94–100.
[63] Y. Liu, T. Pan, L. Zhang, D. Yu, Y. Ge, Kinetic modeling of diffusion mobilities in bcc Ti-Nb alloys, J. Alloy. Compd. 476 (2009) 429–435.
[64] W. Chen, Interdiffusion and atomic mobility in bcc Ti-rich Ti-Nb-Zr system, Calphad 60 (2018) 98–105.
[65] K. Otsuka, C.M. Wayman, Shape Memory Materials, Cambridge University Press, Cambridge, 1999.
[66] K. Bhattacharya, Microstructure of Martensite: Why It Forms and How It Gives Rise to the Shape-Memory Effect, Oxford University Press, Oxford, 2004.
[67] A.G. Khachaturyan, Theory of Structural Transformations in Solids, John Wiley & Sons, New York, 1983.
[68] H. Ikehata, N. Nagasako, T. Furuta, A. Fukumoto, K. Miwa, T. Saito, First-principles calculations for development of low elastic modulus Ti alloys, Phys. Rev. B 70 (2004), 174113.
[69] F. Findik, H.M. Flower, Morphological changes and hardness evolution in Cu-30Ni-5Cr and Cu-45Ni-15Cr spinodal alloys, Mater. Sci. Technol. 9 (1993) 408–416.
[70] X. Xu, J. Odqvist, M.H. Colliander, S. King, M. Thuvander, A. Steuwer, P. Hedström, Effect of cooling rate after solution treatment on subsequent phase separation during aging of Fe-Cr alloys: a small-angle neutron scattering study, Acta Mater. 134 (2017) 221–229.
[71] D.A. Porter, K.E. Easterling, M.Y. Sherif, Phase Transformations in Metals and Alloys, CRC Press, New York, 2009.
[72] U. Dahmen, Orientation relationships in precipitation systems, Acta Metall. 30 (1982) 63–73.
[73] D. Minami, T. Uesugi, Y. Takigawa, K. Higashi, First-principles study of transformation strains and phase stabilities in α'' and β Ti-Nb-X alloys, J. Alloy. Compd. 716 (2017) 37–45.
[74] W. Mei, J. Sun, Y. Wen, Martensitic transformation from b to α' and α'' phases in Ti-V alloys: a first-principles study, J. Mater. Res. 32 (2017) 3183–3190.
[75] P. Wang, M. Todai, T. Nakano, β-phase instability in binary Ti-*x*Nb biomaterial single crystals, Mater. Trans. 54 (2013) 156–160.
[76] D. Wang, S. Hou, Y. Wang, X. Ding, S. Ren, X. Ren, Y. Wang, Superelasticity of slim hysteresis over a wide temperature range by nanodomains of martensite, Acta Mater. 66 (2014) 349–359.
[77] Y.W. Chai, H.Y. Kim, H. Hosod, S. Miyazaki, Interfacial defects in Ti-Nb shape memory alloys, Acta Mater. 56 (2008) 3088–3097.
[78] Y. Zhou, D. Xue, X. Ding, S. Guo, K. Otsuka, J. Sun, X. Ren, Direct evidence for local symmetry breaking during a strain glass transition, Phys. Rev. Lett. 112 (2014), 025701.
[79] J. Zhang, Y. Mao, D. Wang, J. Li, Y. Wang, Accelerating ferroic ageing dynamics upon cooling, NPJ Asia Mater. 8 (2016) e319.
[80] D. Wang, Y. Wang, Z. Zhang, X. Ren, Modeling abnormal strain states in ferroelastic systems: the role of point defects, Phys. Rev. Lett. 105 (2010), 205702.
[81] Y. Ji, X. Ding, T. Lookman, K. Otsuka, X. Ren, Heterogeneities and strain glass behavior: role of nanoscale precipitates in low-temperature-aged $Ti_{48.7}Ni_{51.3}$ alloys, Phys. Rev. B 87 (2013), 104110.
[82] A. Ahadi, Q. Sun, Stress-induced nanoscale phase transition in superelastic NiTi by *in situ* X-ray diffraction, Acta Mater. 90 (2015) 272–281.
[83] J. Zhu, H. Wu, X. Yang, H. Huang, T. Zhang, Y. Wang, S. Shi, Dissecting the influence of nanoscale concentration modulation on martensitic transformation in multifunctional alloys, Acta Mater. 181 (2019) 99–109.
[84] Y. Wang, X. Ren, K. Otsuka, A. Saxena, Temperature-stress phase diagram of strain glass $Ti_{48.5}Ni_{51.5}$, Acta Mater. 56 (2008) 2885–2896.
[85] T. Omori, K. Ando, M. Okano, X. Xu, Y. Tanaka, I. Ohnuma, R. Kainuma, K. Ishida, Superelastic effect in polycrystalline ferrous alloys, Science 333 (2011) 68–71.

[86] S.M. Ueland, C.A. Schuh, Transition from many domain to single domain martensite morphology in small-scale shape memory alloys, Acta Mater. 61 (2013) 5618–5625.
[87] J. Zhu, D. Wang, Y. Gao, T.Y. Zhang, Y. Wang, Linear-superelastic metals by controlled strain release via nanoscale concentration-gradient engineering, Mater. Today 33 (2020) 17–23.
[88] Y. Wang, A.G. Khachaturyan, Multi-scale phase field approach to martensitic transformations, Mater. Sci. Eng. A 438-440 (2006) 55–63.
[89] Y. Wang, A.G. Khachaturyan, Three-dimensional field model and computer modeling of martensitic transformations, Acta Mater. 45 (1997) 759–773.